Design of Capacitive Micro-Electro-Mechanical-Systems (MEMS) Accelerometer, Considering Residual Stress, Temperature Variations and Thermoelastic Damping

Author
Muhammad Ahmad Raza Tahir
00000278052

Supervisor
Dr. Muhammad Mubasher Saleem

DEPARTMENT OF MECHATRONICS ENGINEERING
COLLEGE OF ELECTRICAL & MECHANICAL ENGINEERING
NATIONAL UNIVERSITY OF SCIENCES AND TECHNOLOGY
ISLAMABAD
April, 2021

Design and Analysis of a dual axis Differential Capacitive MEMS Accelerometer using SOI-MUMPs Fabrication Process

Author

Muhammad Ahmad Raza Tahir

00000278052

A thesis submitted in partial fulfillment of the requirements for the degree of

MS Mechatronics Engineering

Thesis Supervisor:

DR. MUHAMMAD MUBASHER SALEEM

Thesis Supervisor's Signature:

DEPARTMENT OF MECHATRONICS ENGINEERING

COLLEGE OF ELECTRICAL & MECHANICAL ENGINEERING

NATIONAL UNIVERSITY OF SCIENCES AND TECHNOLOGY, ISLAMABAD

April, 2021

Declaration

I certify that this research work titled "*Design and Analysis of a dual axis Differential Capacitive MEMS Accelerometer using SOI-MUMPs Fabrication Process"* is my own work. The work has not presented elsewhere for assessment. I have properly acknowledged / referred the material that has used from other sources.

Signature of Student
Muhammad Ahmad Raza Tahir
00000278052

Language Correctness Certificate

This thesis has been read by an English expert and is free of typing, syntax, semantic, grammatical and spelling mistakes. Thesis is also according to the format given by the university.

Signature of Student

Muhammad Ahmad Raza Tahir

00000278052

Signature of Supervisor

Copyright Statement

Acknowledgements

Above all else, acclaims and gratitude to Allah Almighty for his showers of blessings for the duration of the life and to finish this examination work effectively

I might want to communicate my profound and earnest gratitude to my research supervisor Dr. Muhammad Mubasher Saleem (Associate HOD, Department of Mechatronics Engineering, College of E&ME, NUST) for giving me the chance to do the exploration and giving priceless direction all through the research. His elements, vision, genuineness and inspiration profoundly motivated me. He has shown me the procedure how to do the exploration and furthermore the technique how to introduce the work as unmistakably as could be expected under the circumstances. I am grateful for what he had offered me. Besides, I am also thankful for his friendship and empathy. I might likewise want to thank Dr. Umar Shahbaz Khan and Dr. Amir Hamza for guiding me through thesis and evaluation committee.

I am extremely grateful to my parents for their continuous support, love, care and sacrifices to make me prepared for the future through education. I am very much thankful to my siblings for their love, prayers and continuous support to complete this research.

I am also very much thankful to the Department of Mechatronics Engineering and my University, NUST to consider my services and offer me this MS under the career development program.

I dedicate this work to my respected parents for nursing me throughout the life with affections and love and my beloved siblings who always inspired me to do this great accomplishment

Abstract

This paper presents the design of two capacitive MEMS accelerometers while following two different fabrication process constraints. The first accelerometer is designed according to the design specifications of Silicon-on-Insulator Multi-User MEMS Processes (SOIMUMPS) fabrication process and the second design follows the MEMS Integrated Design for Inertial Sensors (MIDIS) fabrication process. The focus of this study is to design a dual axis capacitive MEMS accelerometer with low cross-axis sensitivity and high reliability. The effect of thermoelastic damping and residual stresses is observed on the proposed design and its temperature range of -40 to 100 °*C* is characterized. The operating bandwidth of designed accelerometers is 0-400 *Hz* with operating acceleration of ±15 *g* for design 1 and ±50 *g* for design 2. The FEM simulations of these devices is performed in ANSYS and CoventorWare. The capacitive sensitivities of design 1 and 2 are 31.5 *fF/g* and 38 *fF/g* respectively.

Key Words: *MEMS, Accelerometer, Dual axis, Capacitive, SOIMUMPS.*

Table of Contents

List of Figures

List of Tables

Acronyms

MEMS	Micro-electro-mechanical Systems
FEM	Finite Element Method
TED	Thermoelastic Damping
MIDIS	MEMS Integrated Design for Inertial Sensors
SOIMUMPs	Silicon-on-insulator Multi-user MEMS Process
RF	Radio Frequency
CMOS	Complementary Metal Oxide Semiconductor
ENEA	Electrical Noise Equivalent Acceleration
TNEA	Total Noise Equivalent Acceleration

Chapter 1: Introduction

This research work concentrates on the analysis and design of a dual axis capacitive MEMS accelerometer, using SOI MUMPS fabrication process for the inertial navigation application. First, a scope and motivation of the presented work has discussed briefly. Secondly, an introduction of MEMS accelerometer has discussed. Third, the detail of actuation and sensing mechanisms for MEMS accelerometers has discussed in this section.

1.1 Motivation and Scope

The invention of transistors has greatly changed every field of life. The concept of miniaturization of technology has been the key concern of almost all types of industries from last few decades. It has changed every aspect of human life as the size of all the technical products has reduced many times and availability of devices and better functionality are main benefits of this miniaturization. The technology that has attracted many billion-dollar industries is based on silicon micromechanics and known as micro-electro-mechanical systems (MEMS). MEMS technology now has started to impact almost each area of science and technology. In fields as different as entertainment, automotive industry, remote communications, and light wave systems MEMS is progressively getting to be a key technology.

The worldwide growth for MEMS, which incorporates items such as vehicle-airbag frameworks, display frameworks and inkjet cartridges add up to $40 billion in 2006 concurring to Worldwide MEMS/Microsystems Markets and Openings, a investigate report from SEMI and Yole Improvement and was forecasted to reach $72 billion by next few decades [1]. Companies with solid MEMS programs expanded in numerous sizes. Bigger firms specialized in fabricating relatively high volume and easily accessible components or bundled arrangements for consumer markets such as automobile industries, biomedical instrumentation, and advanced gadgets. Little firms, give esteem in imaginative arrangements and assimilate the cost of custom manufacturing with large profit ratios. Both bigger and little companies ordinarily contribute in research and development to investigate the unused MEMS technology.

1.2 Introduction to MEMS

MEMS and the relevant micro machines and microsystems represent the technology that is of microscopic level and particularly having the moving parts. Generally, the MEMS devices consists of the components in the size range of 1 to 100 μm and these devices range from 100 μm to a few mm. The device consists of small moving parts which interact with the surrounding environment and feed these movement changes to a central unit that is called integrated circuit (IC). These values are filtered and passed to the output terminals of the device and can be utilized for data processing and signal condition in the attached units. Figure1.1 shows the dimensions of the MEMS devices in comparison with other devices.

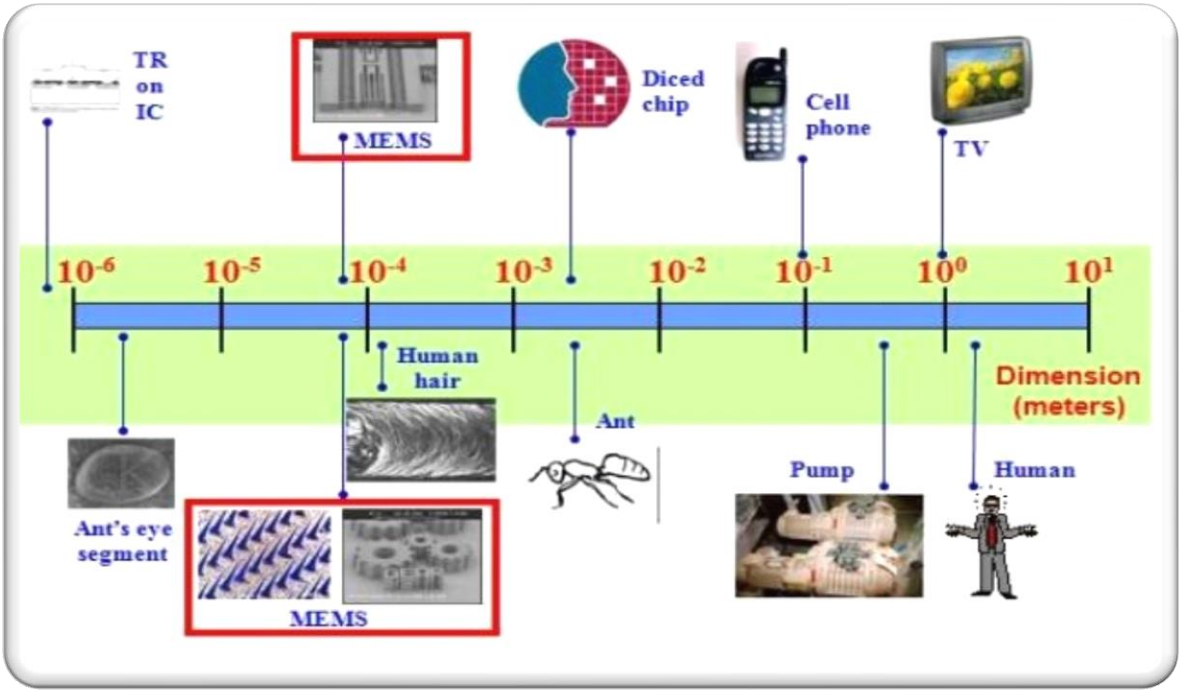

Figure 1.1: Size comparison of MEMS devices with other things.

The revolution of MEMS technology is based on the development of integrated circuit technology and the sensing and actuating devices of MEMS are fabricated on the same chip along with the integrated circuit. After the successful testing and field operation of these devices, governments and industries have started promoting this technology and investing heavy investment is being utilized for the availability of MEMS technology. As a result of progress in the research in this field many fabrication processes have been developed by different research groups worldwide. A number of MEMS devices that are in successful practical use now, have been developed by silicon material and using different fabrication techniques like bulk micromachining, surface micromachining, lithography and SOIMUMPs. Fabrication of these devices under batch fabrication, small in size, low in price and the most important one the reliability are the basic features of these devices.

1.3 MEMS Applications

The MEMS technology has revolutionized almost every area of human life ranging from smaller devices like microphones to large navigation inertial units like drones and air planes. These devices find their applications in a variety of fields like biomedical, electronics devices, automobile, communication and defence field. The use of MEMS devices is common now days as inertial devices for navigation, air conditioning, brake force sensors, fuel level detection sensors, air bag sensors, ink jet printers, pressure monitoring devices, portable devices, RF switches and relays, small health monitoring devices.

1.4 Introduction to MEMS Accelerometer

The word "*accelerometer*" refers the acceleration measurement device. The accelerometer is used for the measurement of acceleration in a variety of devices. The MEMS accelerometer is the miniaturized form of this device and is being used in smart phone and other application for navigation and control purposes. These MEMS accelerometers are configured to measure variations in force arising from positioning, fall, motion, tilt, shock and vibration. There are main two types of accelerometers i.e. single axis MEMS accelerometers and dual axis MEMS accelerometers.

1.4.1 Single Axis MEMS Accelerometer

Single axis MEMS accelerometers have set up ground for vast number of application in several fields from aeronautics to consumer products and 1-axis accelerometer are mostly used in automotive industry due to their high ranges. Despite that, single axis MEMS accelerometers are used to measure the lateral acceleration in electronic stability control (ESC) and automotive safety devices to provide support to drivers to maintain control of their automobiles under uncertain driving situations. Some examples of single axis MEMS accelerometers that are currently being used in automotive safety devices as airbag car crash detection sensors.

1.4.2 Dual Axis MEMS Accelerometer

Due to one dimension of single axis MEMS accelerometer, the performance of these accelerometer was not satisfactory that's why the paradigm has shifted from 1-axis to 2-axis and 3-axis based MEMS accelerometers for better accuracy. Now researchers have been working on dual-axis MEMS accelerometer designs and considering all pros and cons such as cost and performance. The dual axis MEMS accelerometer can be made either by combining two 1-axis MEMS accelerometer or by using a single chip design. The former design however results in greater assembling cost, more possibility of misalignment defects and larger device footprint. In contrast, the single chip design overcomes many of these problems with satisfactory performance [2].

1.5 Microfabrication Process

To fabricate the MEMS devices, different fabrication processes are available. These fabrication processes differ from each other on the basis of material used in fabrication of MEMS devices, type of the device, feature size and the cost involved**.** MUMPs stands for multi-user MEMS process.

1.5.1 LIGA

The acronym LIGA, stands for Lithographie (lithography), Galvanoformung (electroplating) and Abformung (molding). LIGA is one of the MEMS fabrication technique, usually used to produce high aspect ratio designs and structures. Two main types of LIGA fabrication technologies are available, X-ray based and UV based LIGA techniques. For high aspect ratio, X-ray based fabrication is used while for low aspect ratio, UV based fabrication is used for designs and which is more commonly used. This process consists of three main steps: (a) Lithography, (b) electroplating and (c) molding [3].

1.5.2 Metal-MUMPs

The process of Metal-Mumps fabrication uses a metal electroplating to fabricate MEMS devices. Nickel, a metal is used for whole device fabrication in this process. Few MEMS devices like microgrippers have been fabricated using this process [4]. However, Metal-Mumps is not suitable for fabricating the devices with biomedical applications, as of high coefficient of thermal conductivity. High temperatures could damage the object under manipulation.

1.5.3 Poly-MUMPs

Poly-MUMPs stands for polysilicon multi-user MEMS process. MEMS sensors are fabricated using the process of Poly-MUMPS. It has three layers, one of the layers is the metal layer and the other two layers are sacrificial layers. In this process about seven layers can be formed using up to eight masks. 2 μm is the minimum feature size for this process. Silicon have very different properties from polysilicon [5].

1.5.4 SOIMUMPs

A standard and commercially available, low cost process for the fabrication of microstructures is available and is known as the *Silicon-On-Insulator-Multi-User-MEMS* micro level fabrication process (SOIMUMPs) offered by a very well-known and a reliable foundry MEMSCAP Inc. located in United States of America (USA). In this process the substrate under the moveable structures get removed during the etching process and thus this process allows the least air damping. The attribute of fabricating the high aspect ratio micro-structures make its very suitable for the fabrication of the high-performance MEMS devices. Figure 1.2 represents the cross-sectional view of the SOIMUMS process [6].

Figure 1.2: MEMSCAP SOIMUMPs fabrication process cross-section view displaying all the layers [6]

The process has 04 masks for patterning on Silicon-On-Insulator (SOI) wafer and its etching. In the figure 1.6, the doped polysilicon structural layer shown in red color and this coating is fixed against the substrate with the help of oxide layer. Adjacent metal pads are electrically isolated by introducing the grooves in the structural layer. As per the designed rules of this process as mentioned in the SOIMUMPs design handbook [6], the thickness of the silicon layer could be 25±1 μm with the thickness 2±0.1 μm for oxide layer and 400±5 μm of handle wafer (substrate). The minimum feature width of the structure must be 6 μm for the structure length of 200 μm and above. The design deficiencies of the SOIMUMPs manufacturing process puts certain restrictions on the designers. Following design constraints/limitations have been considered during the proposed design of the micromachined accelerometer.

Limitation-1: No electrical lines run across the trenches in the device due to the non-arability of top and bottom cap after etching. Electrode pads could not be the part of the design as they cannot be attached to the inner electrodes. Due to these constraints' designers have only choice of the in-plane sensing and actuation techniques.

Limitation-2: Due to the etching process the bottom cap is missing and hence do not allow the central anchor to be designed in the device as shown in the figure 1.3. Therefore, the proposed design of the accelerometer in comparison to the traditionally available accelerometers in literature differs and we cannot enclose the inner most mass within another mass which is against the design rules of SOIMUMPs fabrication guidelines.

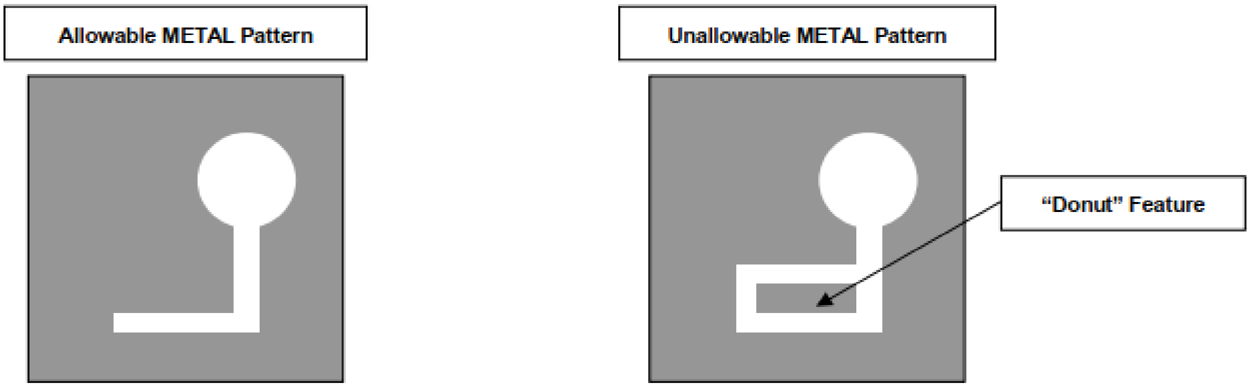

Figure 1.3: Allowable and unallowable feature for metal masking in the SOIMUMPs fabrication process [6]

Limitation-3: Figure 1.6 shows the structural layer in red color made of silicon where the device is patterned. Less than the 33% of the chip area should be etched, which limits the designer to have a certain amount of the gap with in the structures and the number of folds of the springs. The designer has to reduce the unused area and also need to reduce the air gaps between the masses.

Table 1: Material properties for SOIMUMPs TM fabrication process obtained from the CoventorWare material repository.

Material Properties (Units)/Materials	**Silicon**
Young's Modulus GPa	169
Poison Ratio	0.29
Density $(\mathrm{Kg/m^3})$	2500

1.6 Actuation and Sensing Mechanisms in MEMS Devices

To drive the device an actuation mechanism is needed, similarly to calculate the output of the device a sensing mechanism have to be placed. Depending upon the working principles of sensors and actuators different types of mechanism are available in literature.

1.6.1 Actuation Mechanisms

Actuation mechanisms could be broadly classified in to five categories depending upon their working principles which include electrostatic, Electro-thermal, piezoelectric, electromagnetic and the shape-memory-alloy actuators.

In the Electro-thermal actuators [7,8] the force generated is dependent on the thermic expansion of the substance. With extremely small exciting voltages they have capability to generate larger displacements. Due to the limitations of the working temperature range, temperature sensitive objects could not use these types of actuators. The electrostatic actuators [9,10] have the low power consumption, high frequency response and having no hysteresis. however, they need the high voltages to operate. There are two different configurations of the electrostatic actuators, the one is transverse and the second one is lateral comb drives. Electromagnetic actuators have the fast and quick response, having high response and their control is easy. They offer large displacements but their large physical size is the major issue. The piezoelectric actuators offer large output force with very compact dimensions and having good operational bandwidth. But these actuators offer very small displacements which limits its use in extensive applications. Finally, the shape memory alloy actuators [11] have large deformations, high working density and high recovery force. But they have very slow speed and hence low efficiency. Table 2 represents the summary of the actuators used in MEMS applications.

Table 2: Actuation mechanisms and their Comparison [12]

Actuator type	**Working principle**	**Pros**	**Cons**	**Example**
Electro-thermal	Thermal expansion	Large displacement low voltage dimension	High working temperature	[13,14]
Electrostatic	Electrostatic force	Frequency response is fast Power consumption is low No hysterics	Dimensions are large Problems of Pull-in Circuits are complicated	[15,16]

Shape-memory- Alloy	Materials deformation	Flexible low efficiency Frequency response is large	Hysterics Power consumption is large	[17,18]
Piezoelectric	Piezoelectric effect	Large force Good operational bandwidth	Displacement	[19,20]
Electromagnetic	Magnetization effect	Displacements are large linear effect Wearing negligible Response is quick Control is easy	Relatively large dimension Difficult to manufacture	[21]

1.6.2 Sensing Mechanisms

Capacitive sensors [22-24] are the sensors that can estimate the force varying from pN to mN level. For high resolution detection they are mostly used with the electrostatic actuators. Capacitive sensors work on the principle of change in capacitance and its measurements. This capacitance changes between the electrodes and the respective stator and this is done by moving the electrode shuttle. High sensitivity, larger bandwidth, large dynamic range and low power consumption are the key features of electrostatic sensors. But they need complex electronics. Electrothermal sensors follow the principle of the heat consumption from the device surface and the surrounding, differential measurement structures are employed for sensing calculations. They have high resolutions with small dimensions. These sensors have large power consumptions and having low response speed [25-27]

Piezo sensing works on the principle of piezoresistive effect and this technique have been widely used in MEMS. The mechanisms of transduction are used which could convert the mechanical distortions into the voltages. [28,29]. In MEMS piezoelectric sensors are used widely as Resonators and transducers. Having the wide measurement range and wider bandwidth but their manufacturing process are very complex.

Table 3: Comparison of different sensing mechanisms used in MEMS. [12]

Sensor Type	**Working principle**	**Pros**	**Cons**	**Resolution**	**Examples**
Capacitive	Capacitive change	High sensitivity Large bandwidth Fast response speed	Large dimension Complicated circuit	μN	[30]
Electrothermal	Resistance change	Small dimension Simple structure High resolution	Low response speed Large consumption	μN	[25-27]
Piezoelectric	Piezoelectric effect	Measurement range is wide Extra voltage not needed Wider bandwidth	Complex manufacturing process Cannot work in high temperature	μN or sub-μN	[31,32]
Piezoresistive	Resistance change	Simple material High bandwidth Large frequency response	Sensitive to ambient temperature Hysterics Large power consumption	mN	[21]

Chapter 2: Literature Review

2.1 Accelerometer Designs

MEMS accelerometers are mostly divided in various types accordingly to this sensing techniques as capacitive, piezoresistive, tunneling, resonant, and thermal devices which are being used as acceleration sensor. The capacitive technique for acceleration measurement provides many advantages over other techniques and these accelerometers have become very attractive for numerous applications [33]. There are several basic performance parameters on which an accelerometer is characterized and its application is decided. These parameters include range, sensitivity, temperature range, cross axis sensitivity, size and bandwidth. The sensitivity of the accelerometer is a major factor which decides its application another main factor is its size and it is the basic purpose of miniaturization of these devices. There are several designs presented in literature which involve their work on these main performance parameters.

Table 4: Single proof mass based multi-axis capacitive MEMS accelerometers.

Reference	Size (length × width) μm^2	Structural layer material and thickness	Configuration	Capacitive-sensitivity in (fF/g)	Cross axis sensitivity (%)	Input range as (±g)
[34]	260 × 260	Si-4μm	Dual axis	0.48	10	30
[35]	400 × 400	SiO_2-4.1 μm	Three axis	2.46	6.6	1
[36]	1700 × 1700	Si-60 μm	Three axis	4.31	6.1	3
[37]	450 × 450	Si-40 μm	Three axis	3	3	6
[38]	8600 × 8600	Si-25 μm	Dual axis	290	2	1
[2]	1600 × 1600	Si-30 μm	Dual axis	80.9	0	10
[39]	4000 × 4000	Si-30 μm	Dual axis	113.5	-	3

Design for a two axis single accelerometer has shown in [34] which, overcomes the cost expenses involved in single axis accelerometers and arranged in perpendicular for dual axis acceleration measurement. The design is capable of measuring acceleration within span of ±30 g and having cross-axis sensitivity as 10%. The accelerometer is designed by using a 4μm silicon structural layer. The springs are designed in the corners and the sensing mechanism is arranged in both x and y-direction. These type of springs help to achieve minimum cross-axis sensitivity.

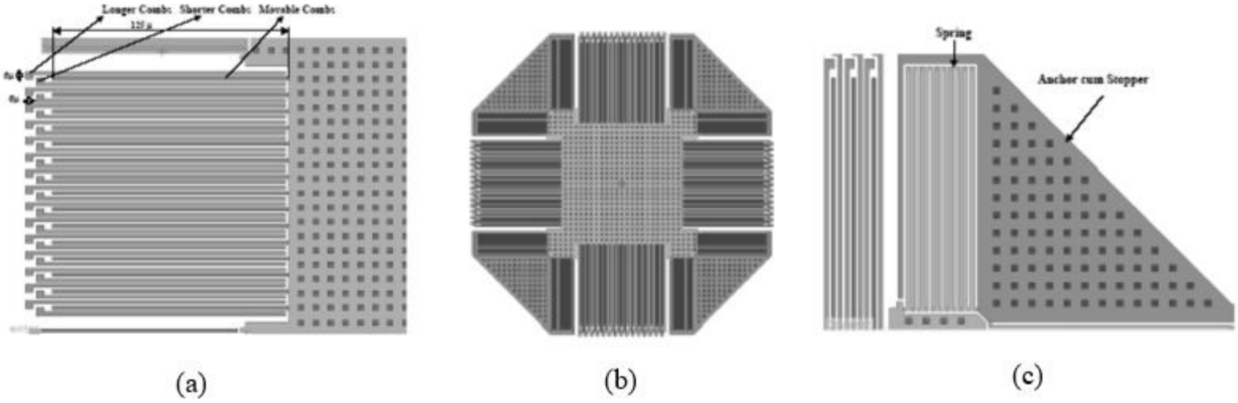

Figure 2.1: Design of accelerometer [34] (a) Sensing combs (b) Schematic (c) Spring

The three-axis capacitive CMOS accelerometer having different capacitive detecting is presented in [35]. The minimum width of metal line is used to defined inside of plane and outside the plane detecting combs. The metal wet etching with post-CMOS process has further improved the capacitance-sensitivity. The multilayer structure of metal allows dielectric stacking in this process.

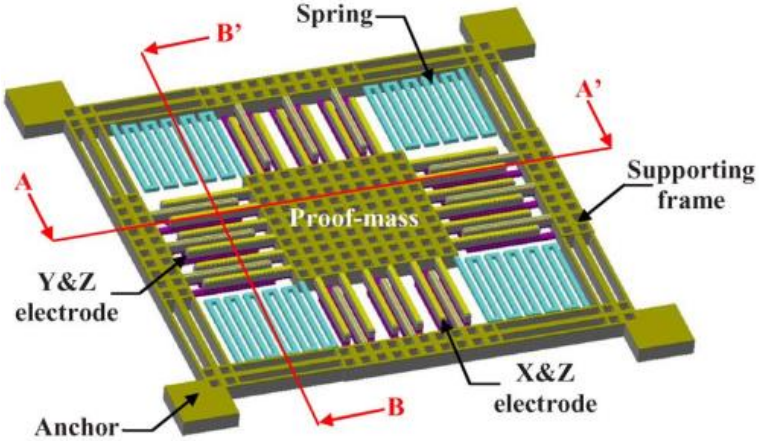

Figure 2.2: Schematic for accelerometer [35]

The idea of single moving-mass capacitance-sensing accelerometer is presented in [36] as shown in Fig. 2.3 which uses the poly silicon MOSBE procedure in [15] for implementation. The Fig. 2.3 show the idea of proposed accelerometer which consists of a rib-moving structure. The stiffness of moving-mass and device is increased using very high-aspect ratio.

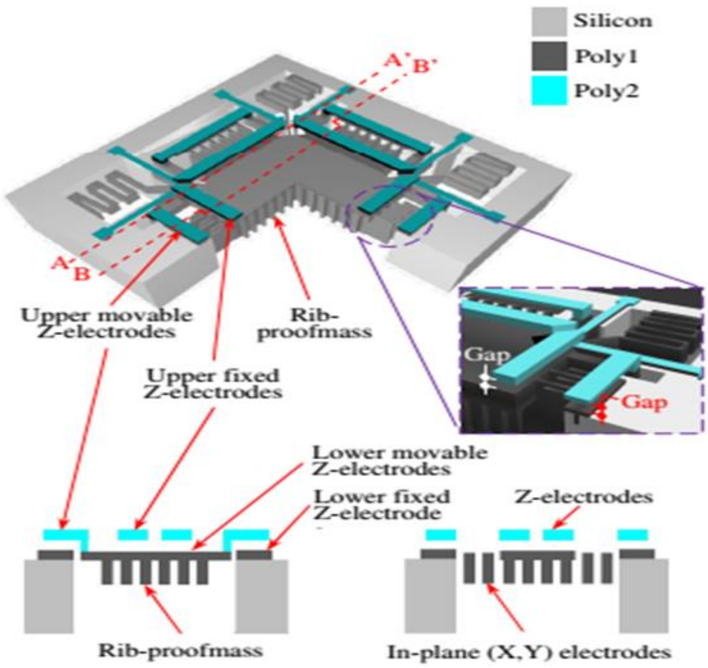

Figure 2.3: Design of proposed three axis MEMS accelerometer [36]

The design, characterization and fabrication of single proof-mass three axis capacitive MEMS accelerometers for low-pressure environments and assembled with high-frequency gyroscopes [37]. This whole system leads to the development of monolithic inertial measuring unit (IMU). These accelerometer works as quasi-static in moderate vacuum pressure and increased squeeze-film damping by using the capacitive nano-gaps. A pendulum structure is designed to reduce the die area and a cross-shaped spring is used to anchor the proof mass. The high resonance frequency is achieved by small capacitive gaps that provide large vibration and shock immunity.

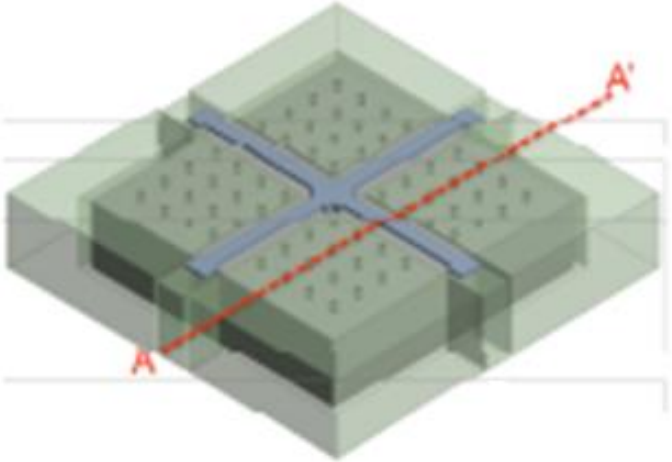

Figure 2.4: three sensing axis accelerometers [37]

A strategy to improve both detectivity, transfer speed of inside plane capacitance micromachined devices for utilizing consistent mechanical amplification, and consequently forestalling the tradeoff between them affectability also transmission capacity [38]. We look at quite possibly the most of touchy capacitance accelerometers while another having enormous thunderous recurrence announced in the writing with the adjusted plans that incorporate removal enhancing consistent instruments involving a similar impression under indistinguishable conditioning. We see a 62% enhancement in affectability while 34% movement in data transfer capacity. The gadget is 25-µm thick with the interfinger hole as extensive as 4 μm. In spite of the effortlessness from microfabrication interaction.

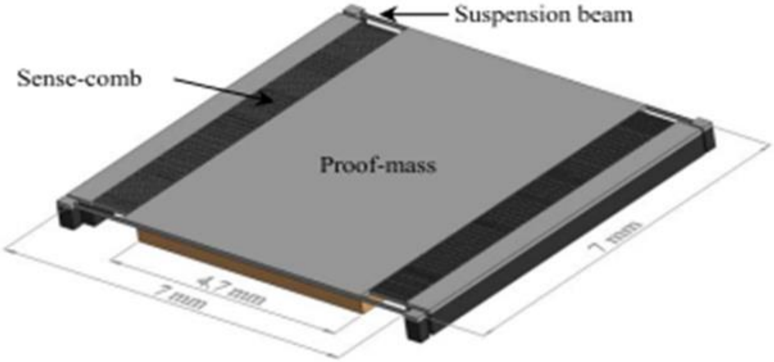

Figure 2.5: The solid model of proposed accelerometer with thick proof-mass [38]

The double axis accelerometer having 0 lateral axis-sensitivity is presented in [2]. By and large, multi-axis accelerometers having one verification mass has numerous levels of opportunity, forming them vulnerable to high-cross-hub affectability. In the report, novel different capacitance plate plot is introduced, which completely dispenses with the in-plane cross-hub affectability at the gadget leveled. The projected accelerometer is profoundly delicate and has a different capacitive digit factor for (80.97) *fF/g*. Also, the out-of-plane movement because of speed increase in the Z-pivot heading is essentially stifled because of the great spring steady around there. The gadget is manufactured in a minimal impression of (1.6×1.6) mm^2 utilizing Globa lFoundries' Inertia Measuring Units (IMU) stage.

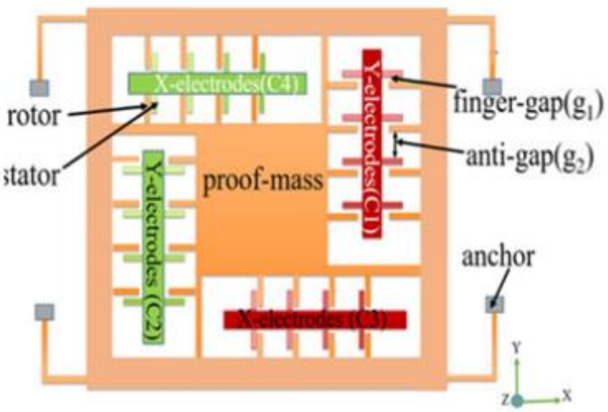

Figure 2.6: Concept diagram of proposed accelerometer [2]

The ideal plan for a two-axis accelerometer designed as low g value applications, alongside its manufacture and testing, is accounted for in [39]. The solid construction was ideally planned dependent on a completely symmetric engineering with a high recurrence proportion between the harsh and the touchy tomahawks. The detecting foundation was planned, thusly, with a configurable search structure for synchronous biaxial capacitive detecting. That accelerometer is created with heavy exactness, tried under 1-g speed increase, both statically and progressively. The comparing dynamic affectability is (1.55) *lm/g*, and capacitance affectability was (113.5) *fF/g*.

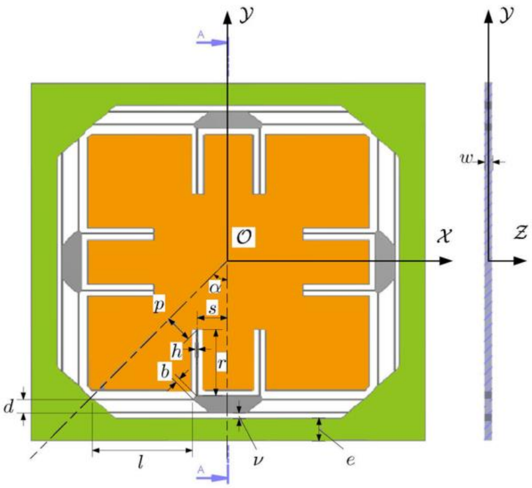

Figure 2.7: Schematic of proposed MEMS accelerome

Chapter 3: Dual Axis Capacitive MEMS Accelerometer Design using SOIMUMPS Fabrication Process

This chapter presents the complete design of the proposed MEMS accelerometer. The estimation of the mechanical springs' stiffness, damping, and capacitance change and cross axis sensitivity through the proposed design is also described.

3.1 Structural Design of the Proposed MEMS Accelerometer

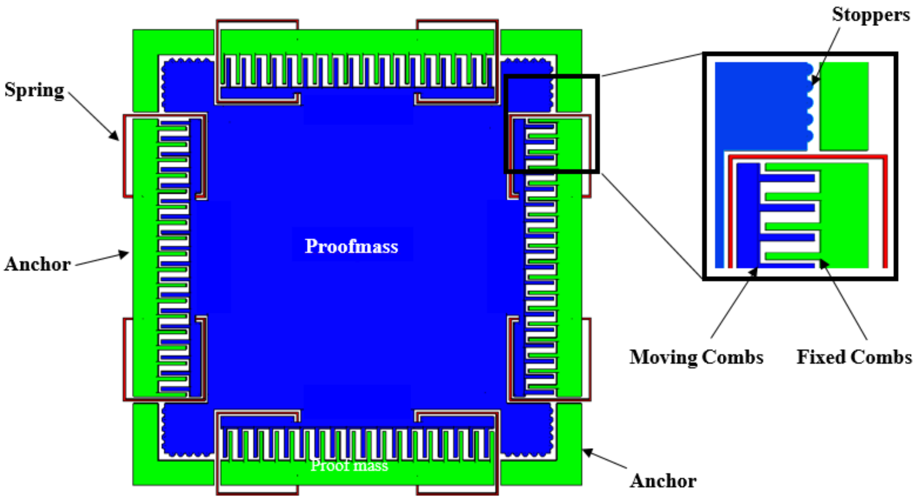

Figure 3.1: Proposed design of dual axis capacitive MEMS accelerometer using SOIMUMPS fabrication process

Figure 3.1 demonstrates the proposed dual axis MEMS accelerometer. The major obstacle in the designing of the proposed MEMS accelerometer was the microfabrication process constraints enforced by the MEMSCAP Inc. USA's low cost SOIMUMPs technique available in the market.[7] As in this method, the Silicon is completely burned through the substrate, so during the designing process the following constraints should be fallen to account: a) in the absence of bottom-side electrode, the out-of the plane displacement of the moving mass cannot be detected and b) the suspension springs and the anchors needs to be positioned at the verge of the design.

Furthermore, thickness for Silicon structural layer should be optimized up to a maximum of 25 µm.

To sense acceleration in x as well as y direction, the structure of the MEMS accelerometer proposed here consist of only simple proof mass. To maximum the displacement in the desired axis and minimize the cross-axis displacement, the suspension beams are created in a square form. The structural design of the suspension springs comprises of two groups of springs coupled on all sides for moving mass and rectangular beams. The capacitance transducing mechanism chosen for the proposed design. The gap and anti-gap configuration [2] was used for rotor and stator parallel plates with a ratio of 3 on the verge of the proof mass. The minimum gap allowed between parallel plates is 2 µm according to the fabrication process constraints. The initial gap of 3.5 µm was kept in order to reduce Brownian noise and squeeze film air damping. Multiple end stoppers were used in a circular form on all the 4 corner ends for the moving mass lead to minimize sudden high-g mechanical shock effect. To attach anchors with proof mass, eight square shaped springs were used. The purpose of the square-shaped springs is to lower the cross axis movement of the proof mass.

3.2 Analytical Modeling of the Proposed MEMS Accelerometer Design

This section deals with the analytical modeling of design 1 of the proposed capacitive MEMS Accelerometer using SOIMUMPS as fabrication process.

3.2.1 Equations of Motion

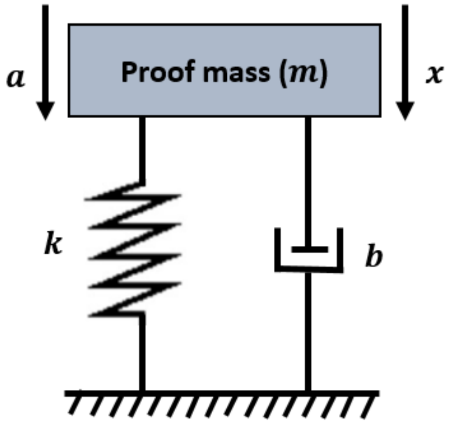

Figure 3.2: Simple mass-spring-damper model for the MEMS accelerometer.

A basic mass-spring-damper displayed in Fig. 3.2 can be used to elaborate the functioning of MEMS accelerometer. The moving mass' equation for the motion for an acceleration a, can be presented as;

$$m\ddot{x} + b\dot{x} + kx = ma\cos\omega t \tag{1}$$

Where m denotes the mass-value of the proof mass, k is the equivalent spring constant of the mechanical springs and c is damping due to the air. The solution for the Eq. 1 is given as;

$$X = \frac{{}^{ma}/_{k}}{\left(\left(1 - \frac{\omega^2}{\omega_n^2}\right)^2 + \left(4\zeta\frac{\omega^2}{\omega_n^2}\right)\right)^{1/2}} \tag{2}$$

where $\omega_n = \left(\frac{k}{m}\right)^{1/2}$ is the input acceleration frequency, ω_n is the natural frequency of the accelerometer and $\zeta = \frac{b}{2m\omega_n}$ is the damping ratio.

3.2.2 Calculation of the Mechanical Stiffness of Suspension Beams

The diagram of a mechanical spring used in designing proposed MEMS accelerometer is shown in Figure 3.3. The spring contains five rectangular beams connected within series manner. The spring-stiffness constant K of a single beam can be given as;

$$K = \frac{E\omega t^3}{l^3} \tag{3}$$

Where *E*, *t*, *l* and *ω* represents young's modulus, length, thickness for beam while width for beam.

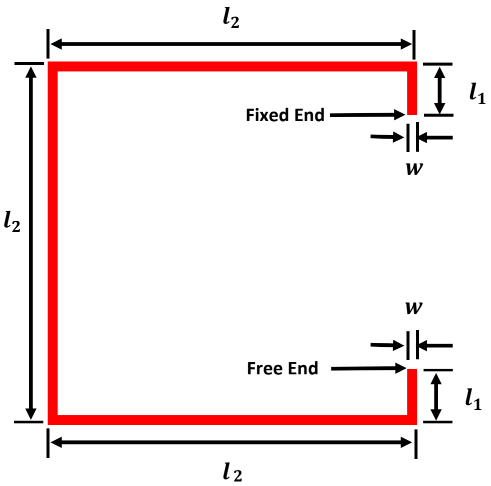

Figure 3.3: Schematic of the C-shaped springs for the design of MEMS accelerometer

Eq. 4 denotes the proof mass' mechanical springs' equivalent spring constant k_{eq} in the lateral direction.

$$k_{eq} = \frac{4Et\omega^3}{2l_1^3 + 3l_2^3} \tag{4}$$

Table 5: Design parameter for proposed dual-axis capacitive MEMS accelerometer.

Parameters	Values

Proof mass dimensions ($l_p \times w_p$)		$2730\ \mu m \times 2730\ \mu m$
Structural layer thickness (t)		$25\ \mu m$
Mass value of the proof mass (m)		$5.05 \times 10^{-7}\ Kg$
Length of parallel-sensing-plates (l_c)		$250\ \mu m$
Width of parallel-sensing-plates (w_c)		$6\ \mu m$
Number of parallel-sensing-plates (n)		86
Overlap length between the stator and rotor plates (L_o)		$245\ \mu m$
Sensing gap width (d_1)		$3.5\ \mu m$
Anti-sensing gap width (d_2)		$10.5\ \mu m$
Length of suspension beams	(l_1)	$80\mu m$
	(l_2)	$665\mu m$
Width of suspension beams (w)		$15\mu m$
Spring constant (k_{eq})		69.18

3.3 Calculation for Differential Capacitance Change

With an input acceleration coming from a laterally direction, the displacement by the proof mass of the accelerometer from its mean position is based on the acceleration magnitude and can be calculated by transforming it into an observable form. As described earlier, the capacitance change that occurs due to proof mass displacement can be estimated as given in Eq. 5;

$$c_d = \frac{2x\varepsilon_o L_0 t n(d_2^2 - d_1^2)}{(d_2^2 - x^2)(d_1^2 - x^2)} \tag{5}$$

where vacuum permittivity is denoted by ε_o, number of combs by n, thickness of combs by t_c and d_1 and d_2 are widths of gap and antigap respectively.

3.4 Modal Analysis

The modal analysis of the proposed MEMS accelerometer was conducted using CoventorWare software to estimate the modal shapes of the proposed design. With a natural frequency of 1.493

kHz, the first three modal frequencies along with their shapes for MEMS accelerometer are shown in Figure 3.4. The comparison among these three modes shows that moving-mass displacement is out-of-plane in the first mode while in second and third mode proof mass have pure translational motion. Besides, first mode is isolated from second and third modes with a frequency of 340 Hz. The analysis results from different simulations such as analytical modal, 3D ANSYS simulations and CoventorWare simulations were compiled in the Table. 4. The results from analytical modal and CoventorWare simulations exhibits close symmetry.

Table 4. Comparison of the first three frequency modes for the MEMS accelerometer.

Mode Shape	Analytical Model (kHz)	3D ANSYS Simulation (kHz)	CoventorWare Simulation (kHz)
2nd	1.875	1.837	1.866
3rd	1.875	1.837	1.866

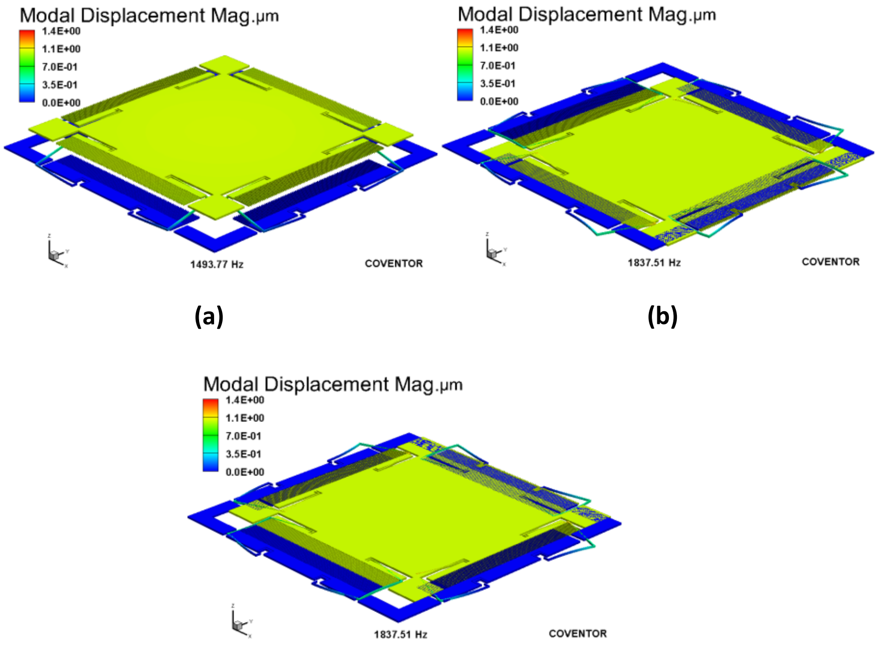

(a) (b)

(c)

Figure 3.4: Mode shapes for the proposed MEMS accelerometer (a) 1st mode (1.493 kHz) (b) 2nd mode (1.837 kHz) and (c) 3rd mode (1.837 kHz)

3.5 Air Damping Analysis

The main energy dissipative mechanism for proposed MEMS accelerometer design is the air damping which can be attributed to squeeze-film air-damping while slide-film air-damping between the stator and rotor parallel plates connected with moving-proof mass. The squeeze film air damping is dominant in the sense axis while slide film air-damping is present within orthogonal axis. The coefficients of squeeze-film air-damping (b_{sq}) and slide-film air-damping (b_{sl}) can be estimated as[40];

$$b_{sq} = \mu_e N l_o t^3 \left(\frac{1}{d_1^3} + \frac{1}{d_2^3} \right) \tag{6}$$

$$b_{sl} = \mu_e N l_o t \left(\frac{1}{d_1} + \frac{1}{d_2} \right) \tag{7}$$

Where N is numbers for stator and rotor parallel-plates, μ_e is effective-coefficient for air-viscosity and l_o is overlap length.

The main energy dissipative mechanism for proposed MEMS accelerometer design is the air damping which can be attributed to squeeze-film air-damping and slide-film air-damping between the stator and rotor parallel plates attached to the proof mass. The squeeze film air damping is dominant in the sense axis while slide-film air-damping is present in the orthogonal axis. The air damping force acting on the proof mass of the MEMS accelerometer can be either viscous or elastic depending on the frequency of the input acceleration. To analyze the effect of the input acceleration frequency and hence strong air-damping scenario in the MEMS accelerometer design, a detailed air damping analysis is carried out in the CoventorWare DampingMM-module. Figure 3.5 shows the effect of increasing input acceleration frequency on both the viscous and elastical spring-damping force. The results show that for low value of input frequency i.e. up to 3 kHz, the viscous air damping is the dominant mechanism and damping force increases linearly with frequency for both slide and squeeze film air damping. However, for high values of the input acceleration frequency, elastical damping-force becomes the dominant energy dissipation mechanism. Hence, for the MEMS accelerometer design since the operating frequency range is 0-400 Hz, the viscous damping force will be main air damping mechanism. The value of the squeeze film and slide film air damping related coefficients got through the FEM analysis are 4.94×10^{-4} and 3.64×10^{-6} respectively. This values are in good correspondence with the analytical values of 2.8×10^{-4} and 7.26×10^{-6} squeeze and slide film air damping coefficients respectively obtained using Eq. 7 and 8.

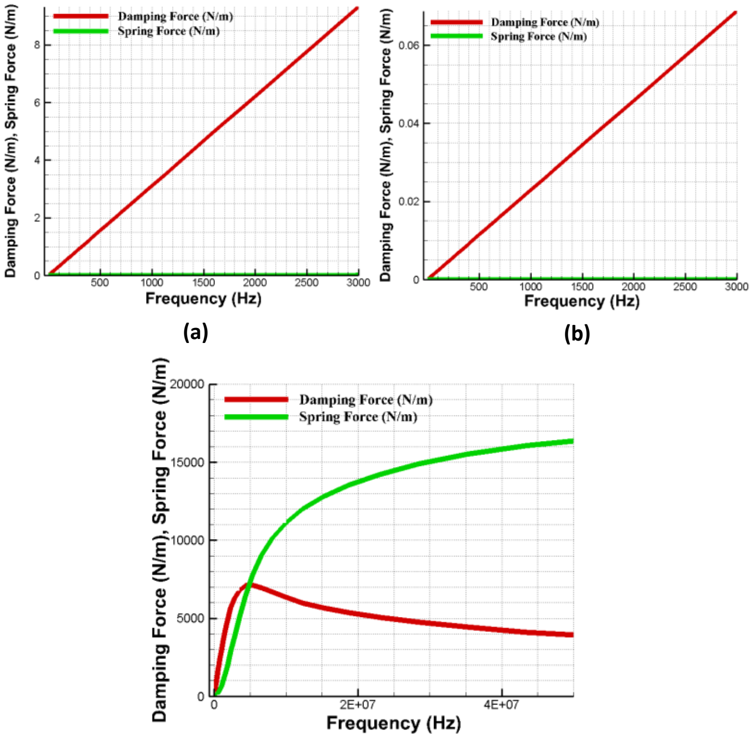

(a) (b)

(c)

Figure 3.5: Effect of input acceleration frequency on the viscous and elastic air damping forces on proof mass (a**)** squeeze-film air-damping for frequency up to 3 kHz (b) slide-film air-damping for the frequency to 3 kHz (c) squeeze-film air-damping while frequency up to 50 MHz

Pull-in voltage analysis for the MEMS accelerometers based on electrostatic transduction mechanism, initially biased voltage has to be applied between the stator and rotor parallel plates for sensing the proof mass displacement in the form of capacitance change corresponding to an input acceleration. Thus, it becomes very important to find the maximum threshold voltage value that can safely be applied a bias to avoid the mechanical damage. The maximum bias voltage value is limited by the pull-in phenomenon. With an applied actuation voltage, the moving parallel plates move towards the fixed plates under effect of electrostatical forces. The voltages value for which the electrostatically strong forces lead to the mechanical restoring forces for suspension-beams can be termed as pull in voltages while respective deflection in the moving plates can be termed as pull in deflection [41]. The pull in value of voltage in case of a gap-antigap based stator and rotor parallel plates in the MEMS accelerometer is given as;

$$V_{pull-in} = \sqrt{\frac{8kd_1^3}{27.l.t.N.\varepsilon}} \tag{8}$$

Where k is the spring constant, d_1 is the initial gap between the moving and dixed plate, l is the overlap length, t is the thickness of parallel plates, ε is the permittivity of free space and N is number of moving and fixed plate pairs. Figure 3.6 shows the results for the proof mass displacement with respect to the applied bias voltage for MEMS accelerometer obtained using CoventorWare MEMS+ module. The results show that the proof mass displacement with respect to applied bias voltage is non-linear and the pull-in voltage value is 6.7 V with corresponding pull-in displacement of 0.64 µm. Thus, for the safe operation of the proposed MEMS accelerometer design, the bias voltage value must be less than 6.7 V.

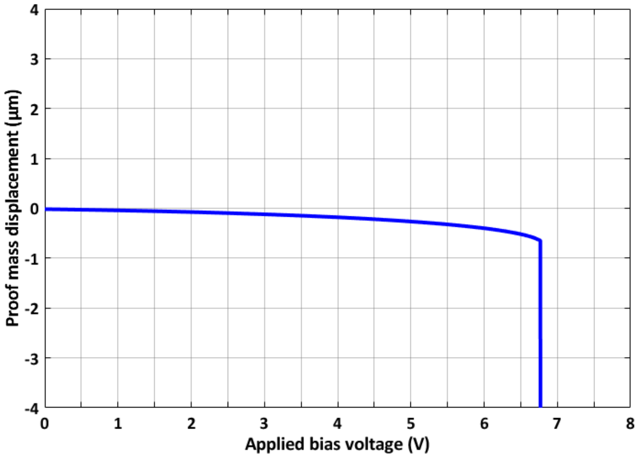

Figure 3.6: Proof mass displacement vs. applied bias voltage graph for the MEMS accelerometer.

3.6 Frequency Response Analysis

To analyze the effect of the varying input acceleration magnitude and frequency values on the displacement amplitude of the MEMS accelerometer proof mass, a frequency response analysis is carried out in CoventorWare MEMS+ module. Figure 3.7 (a) shows that for an input acceleration of 15 g and input frequency matching the sensing mode frequency, the proof mass displacement is maximum with a value of 11.45 μm. This value is much higher than the initial gap of 3.5 μm between the stator and rotor sensing parallel plates attached to proof mass. However, since the MEMS accelerometer is designed to be operated in the frequency bandwidth of 0-400 Hz the value of proof mass displacement in this frequency range is nearly 1.1 μm which is less than the initial gap. Moreover, in the desired operational frequency range the proof mass displacement amplitude is also constant thus avoiding any nonlinearity. Figure 3.7 (b), shows the proof mass displacement amplitude with input acceleration magnitude up to 15 g with an increment of 3 g.

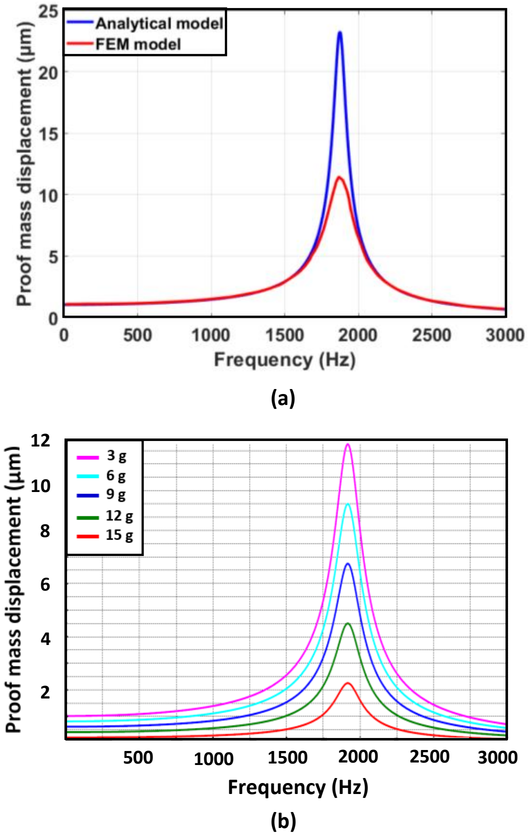

(a)

(b)

Figure 3.7: Frequency response of the MEMS accelerometer (a) input acceleration of 15 g (b) input acceleration in the range of 1 to 15 g.

3.7 Out-of-plane Sagging Analysis

The z-axis deflection in the proof mass of the MEMS accelerometer due to self-weight may result in misalignment between the sensing parallel plates. Thus, a sagging analysis with load equal to the weight of the proof mass is carried out in CoventorWare MEMS+ module. Figure 3.8 shows that maximum z-axis displacement in the proof mass due to self-weight is only 0.16 µm and it is uniform for whole mass. This value is negligible as compared to structural layer thickness of 25 µm thus its effect on the capacitance change between the stator and rotor parallel plates due to change in overlap area can be ignored.

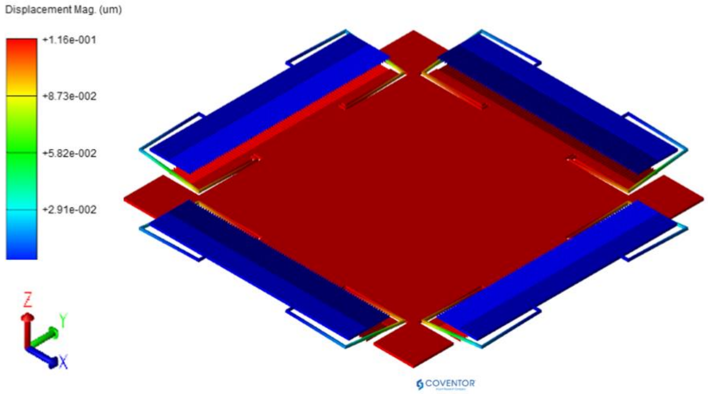

Figure 3.8: Out-of-plane deflection in the proof mass of MEMS accelerometer due to self-weight.

$$Q_{ted}^{-1} = \frac{\Delta_M \omega_n \tau}{1 + (\omega_n \tau)^2} \tag{9}$$

3.8 Thermoelastic Damping

Thermoelastic damping is an intrinsic source of energy dissipation mechanism in thermos-elastic solids due to vibrations induced compressions or extensions. For a beam undergoing bending, alternate temperature profiles are developed across the beam thickness due to presence of time-varying compression and tensile strains on the opposite sides of the beam neutral axis. These temperature gradients lead to irreversible heat flow and hence damping or energy dissipation in beam at a rate dependent on the vibration frequency of the beam. For a beam, undergoing flexural bending, the thermoelastic damping in terms of quality factor can be expressed as [42];

Where $\tau = \frac{C_v b^2}{K\pi^2}$ is the relaxation time, $\Delta_M = \frac{E\alpha^2 T_0}{C_v}$ is the relaxation strength, E is Young's modulus, w_n is resonance frequency, T_0 is the operating temperature, $C_v = \rho C_p$ is specific heat capacity at constant volume, α is coefficient of thermal expansion, C_p is the specific heat capacity at constant pressure, K is thermal conductivity and ρ is the density of the material.The Eq. 9 shows that energy loss factor or quality factor for a vibrating structure strongly depends on the material properties. However, it has been previously reported that material properties of Silicon including α, K and Cp significantly change even in the normal operating temperature range of 250 K to 400 K [43]. To analyze the effect of thermoelestic damping on the quality factor of the MEMS accelerometer, a FEM based detailed nonlinear harmonic analysis is carried out in the Coventorware MemMech module by using temperature dependent properties of the silicon. This analysis considers TED in the solid and moving parts of the 3D model. Figure 3.9 (a) shows the temperature contour plot for the accelerometer at room temperature, due to TED, for an input acceleration of 15 g. The greatest TED induced temperature variations occur in the suspension beams with a temperature of nearly 0.078 K. Figure 3.9 (b) shows the quality factor values for the MEMS accelerometer in the temperature range of -40 ℃ to 100 ℃. The results show that the quality factor increases non-linearly with an increase in the MEMS accelerometer operating temperature with a maximum value of 1.2×10^6 at 100 ℃. The comparison of the Qted obtained through FEM simulation to that calculated using Eq. 9 shows a significant difference. This may be attributed to that fact that the TED model presented in [42] is based on some restrictive assumptions and is valid for simple geometries like thin rectangular beams undergoing pure flexural bending, while for the MEMS accelerometer design, the combination multiple micro-beams as a suspension spring results in a relatively complex deformation behavior.

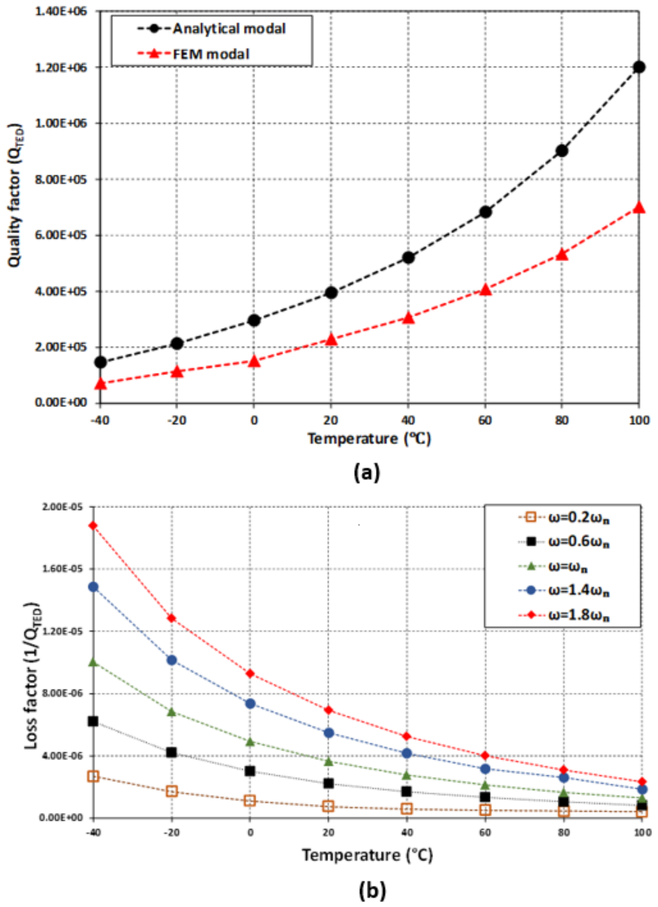

Figure 3.9: (a) comparison of change in Quality factor for Analytical and FEM models with in a temperature range of of -40 ℃ to 100 ℃ (b) Variation in Loss factor value for different frequencies with change in temperature

3.9 Residual Stress Analysis

Residual stresses are intrinsic stresses of the material, which remain in that solid material after the original cause of stress is removed. The Experimental results of diagnostic structures, utilised to determine the characteristics of SOIMUMPs fabrication process, show that the in-plane residual stresses for this process are less than 20 MPa [44]. In microsystems the main cause of residual stresses is the rise and fall of temperature during fabrication process. In the annealing process when the material cools down all the stresses due to temperature are not released. Due to these residual stresses the stiffness of the material is increased and consequently there is s rise in natural frequency. To analyse the effects of residual stresses in proposed MEMS accelerometer, DC sweep is carried out in CoventorWare Analyser module with residual stress value of 20 MPa and results are shown in the Fig. 3.10 (a). Simulation result shows that there is a contraction in the springs of 5 nm in inward direction. As the structure is symmetric, there is a minimal change in the position of the proof mass and combs. From the graph in Fig. 3.10 (b) it is quite clear that the capacitance change decreases on both side of 0 value of stress gradient.

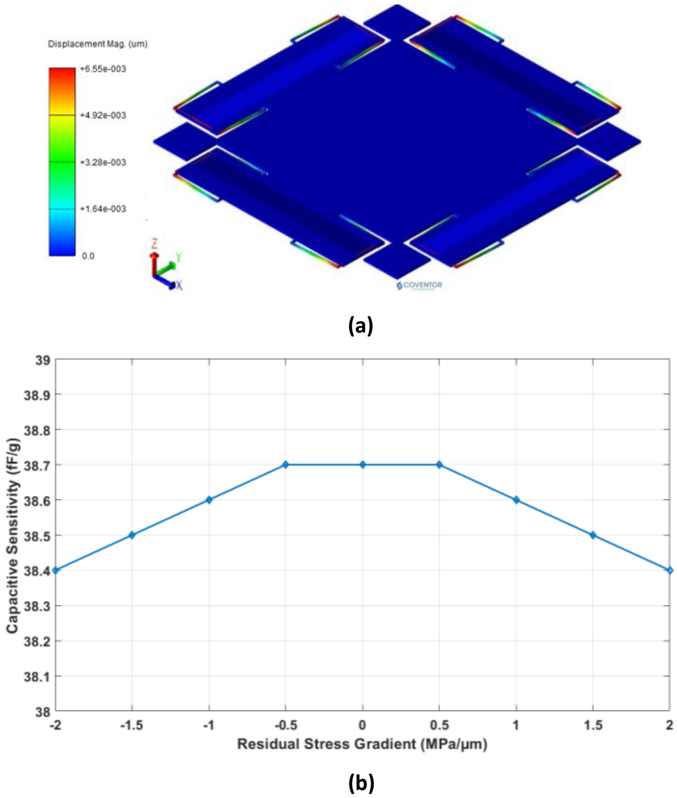

Figure 3.10: (a) Residual stress analysis carried out in CoventorWare Analyzer module (b) Effect of residual stress gradient on change in capacitance sensitivity

3.9 Effects of Temperature on Performance Parameters

3.9.1 Operating Input Acceleration Range of MEMS Accelerometer at Room Temperature

The range of accelerometer is decided by the occurrence of pull-in phenomenon between the combs. The bias voltage that is applied between the fixed and moving combs is 2.25 *V*, which is a constant value provided by the readout IC MS3110^{TM}. In CoventorWare's MEMS+ module a *DC* sweep is carried out to find the maximum operational range of acceleration, a bias voltage is applied and an acceleration sweep from 0 to 50 *g* is given to find the value of acceleration at which pull-in occurs. The result of this analysis shows that value to be 34 *g* as shown in Fig 3.11, which means that accelerometer when biased with 2.25 *V* can operate for acceleration range of ±34 *g*, applied at room temperature. This operating range changes with change in temperature because smaller gap does not remain constant with thermal expansion and contraction of the accelerometer.

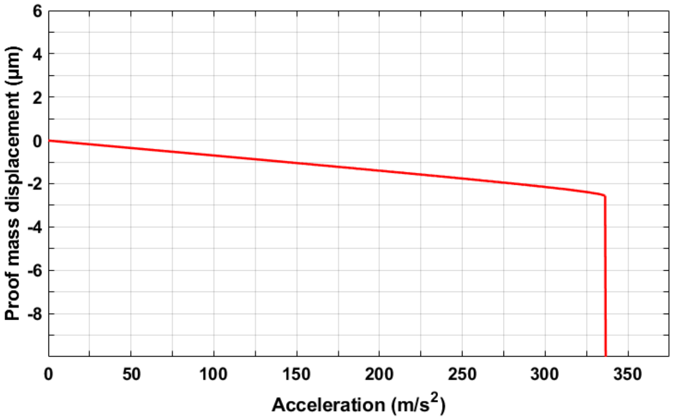

Figure 3.11: Analysis for maximum acceleration range at standard conditions (25 °C and 101.32 kPa)

3.9.2 Variation in Operating Input Acceleration Range with Change in Temperature

The operating range of an accelerometer can be affected by a change in temperature due to the fact that expansion or contraction changes the gap between combs, this results in a lower or higher value of acceleration at which pull-in occurs, consequently increasing or decreasing the accelerometer range. For non-differential configurations a general rule is, that low temperatures will result in contraction hence increasing the gap between rotor and stator combs which results in an increased range whereas for high temperatures the opposite is true. But in the case of differential configuration, the smaller gap is always reduced, since increase in the gap on one side results in an equal decrease on the other side. This means that in the case of differential sensing, smaller gap is always reduced, due to either increase or decrease in temperature, this phenomenon is shown in Fig. 3.12. The initial gap d_1 between fixed and moving combs on both sides is 3.5 *µm* as shown in

Fig. 3.12 (c). As the temperature decreases down to -40 ℃, due to the contraction of the structure, smaller gap d_1 changes from 3.5 μm to 3.67 μm in right side combs but at the same time it is reduced from 3.5 μm to 3.33 μm in left side combs as shown in Fig. 3.12 (a). When the temperature is raised to 100°C due to thermal expansion, the gap d_1 decreases from 3.5 μm to 3.25 μm in right side combs and increases from 3.5 μm to 3.75 μm in left side combs as shown in Fig. 3.12 (b).

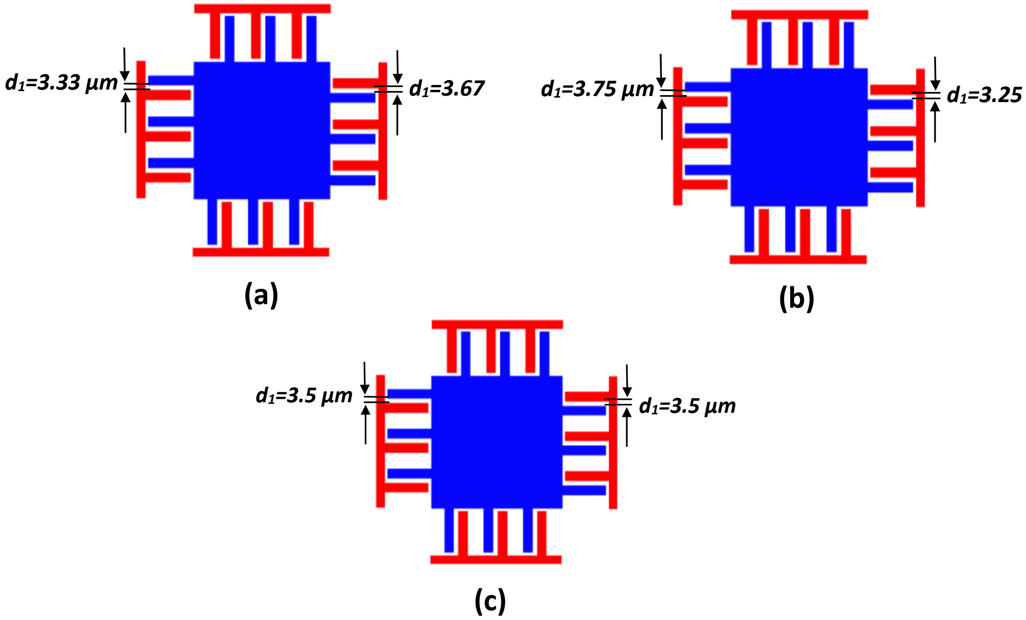

Figure 3.12: Schematic depicting the change in gap size with temperature (a) at -40℃ (b) at 100℃ (c) at 20℃

Figure 3.13 shows the variation of safe operating acceleration with change in temperature. At room temperature the safe operational range is 33.9 g. For a lower temperature of -40℃ safe operational acceleration decreases to 30.9 g and for 100℃ it is 29.9 g.

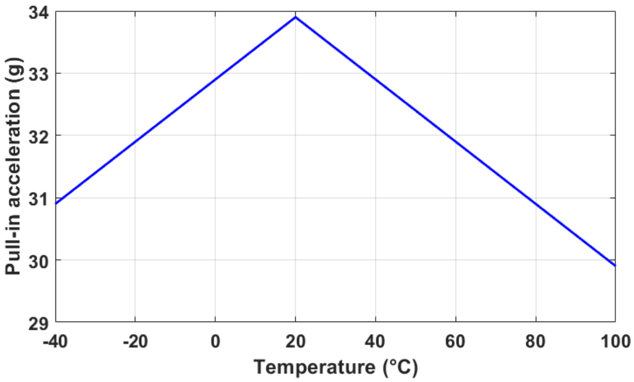

Figure 3.13: Change in acceleration range with respect to temperature

3.9.3 Thermal Effects on Packaging of MEMS Accelerometer

Figure 3.14 shows the change in smaller gap d_1 for a temperature range of −40 ℃ to 100 ℃, it depicts the variations in three different scenarios. At first, only the device layer is subjected to different temperatures to observe the variation in smaller gap d_1 then the device along with the substrate is observed at different temperatures and finally the packaged device is subjected to a range of temperatures. The results showed that when thermal conditions are applied only on device layer, the gap size variations are significant but as the substrate is also included in the simulation the change in gap size become less prominent and this trend continues when the completely packaged devices is simulated. When thermal conditions are applied only for device layer the movement of rotor combs with respect to fixed combs is significant. When simulation is carried out for device layer with substrate the relative gap between the rotor and stator combs becomes less prominent as the substrate restricts the the movement of fixed combs. The least relative change is observed in gap size between fixed and moving combs when device is placed on a plastic die and thermal behaviour is observed.

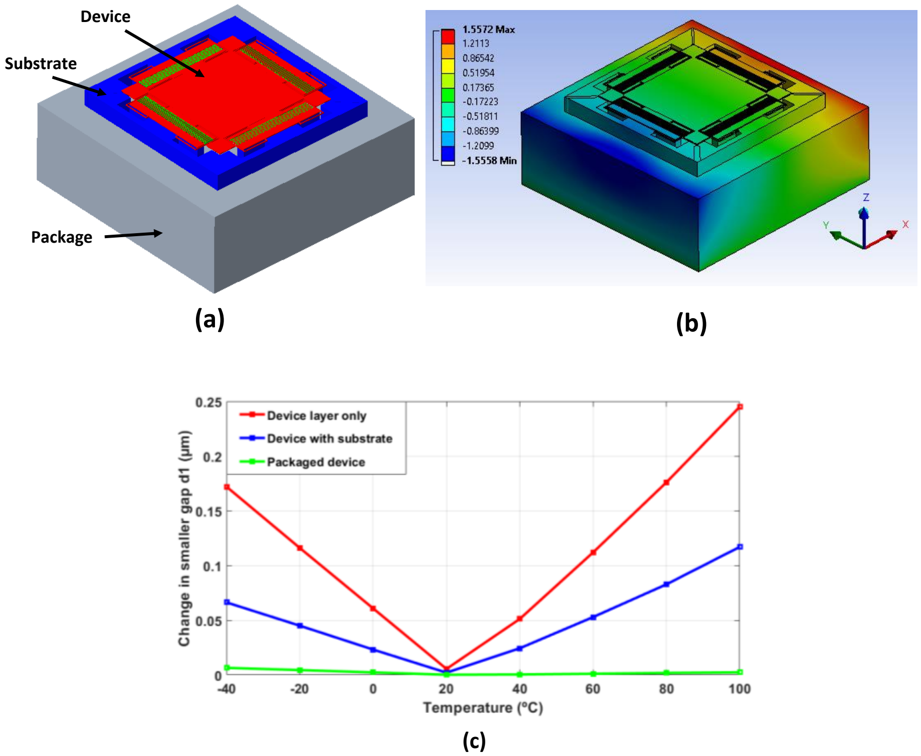

(a) (b)

(c)

Figure 3.14: (a) 3D model of packaged device (b) Thermal analysis for packaged device carried out in ANSYS (c) Graph of change in smaller gap (d_1) Vs temperature for device layer, device layer with substrate and packaged device

3.9.4 Effect of Temperature on Young's Modulus

As the variation in temperature directly affects the material characteristics, which can be observed by analyzing the change in Young's modulus E of a material. A semi-empirical relationship to estimate the change in Young's modulus of a material against different temperatures is developed by Wachtman, and is given as [45],

$$E(T) = E_0 - BT\, exp\left(-\frac{T_0}{T}\right) \qquad (10)$$

Where B and T_0 are constants, which are correlated with Grueneisen parameter and Debye temperature respectively. E_0 and $E(T)$ represent values of Young's modulus at 0 K and required temperature T respectively. For Silicon, the values of B and T_0 are estimated to be 15.8 MPa 317

K respectively [46].

Figure 16 (a) shows the effect of variation in temperature on the Young's modulus of material based on Eq. 13. As the temperature is varied from $-40\,^{\circ}\mathrm{C}$ to $100\,^{\circ}\mathrm{C}$, the Young's modulus decreases nonlinearly. For these different values of Young's modulus, dynamic performance of the proposed MEMS accelerometer is analyzed in CoventorWare MEMS+ module by carrying out Harmonic analysis with 15 *g* input acceleration and results are shown in Fig. 3.15 (b)

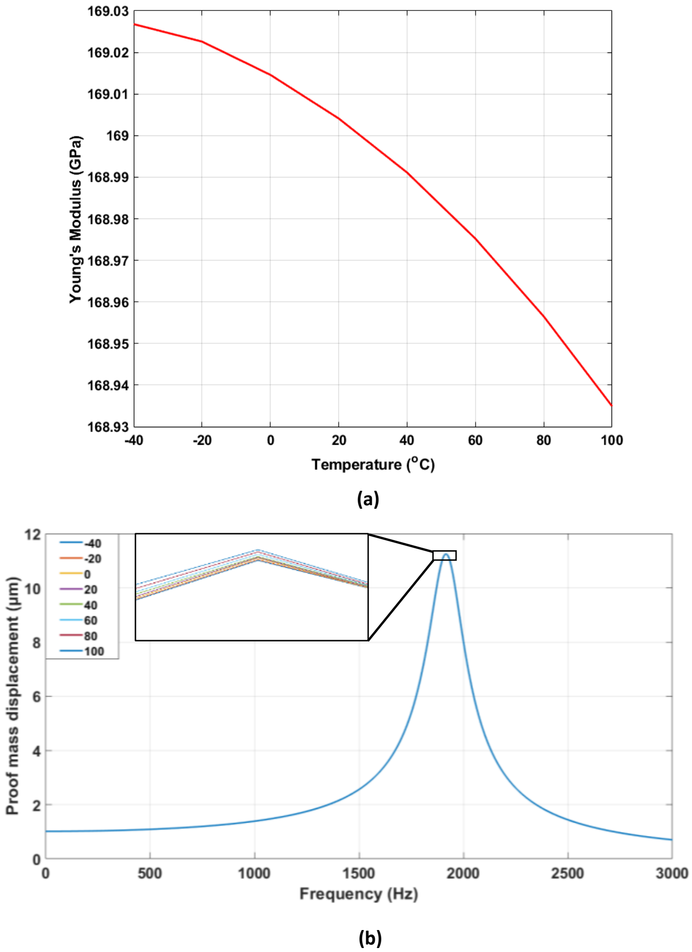

(a)

(b)

Figure 3.15: (a) Effect of Temperature on Young's modulus of device layer material (b) Harmonic analysis of proposed MEMS accelerometer for different value of Young's modulus with respect to temperature change

3.9.5 Effect of Temperature and Pressure on Damping

The change in temperature has a direct impact on the dynamic response of MEMS accelerometer due to the variation in coefficients of damping. This change in damping value can be attributed to the change in effective viscosity, which is given by the following equation [47];

$$\mu_{ef} = \frac{\mu}{1 + 9.638K_n^{1.1}} \tag{11}$$

Where μ is the viscosity of air, K_n is the Knudsen number which is the ratio of mean free path of the air to the smallest gap in accelerometer structure which is the sensing gap (= d_1) in our case. Figure 3.16 (a) shows the variation in damping coefficient value for a range of temperature from -40 °C to 100 °C. The damping coefficient decreases from $5.05 \times 10^{-4}\ Nm/s$ at -40 °C to $4.66 \times 10^{-4}\ Nm/s$ at 100 °C, indicating a change of 7.5 %. The decrease in the value of loss factor is observed with increase in temperature and the comparison of loss factor for change in temperature at different frequencies is shown in Fig. 3.16 (b).

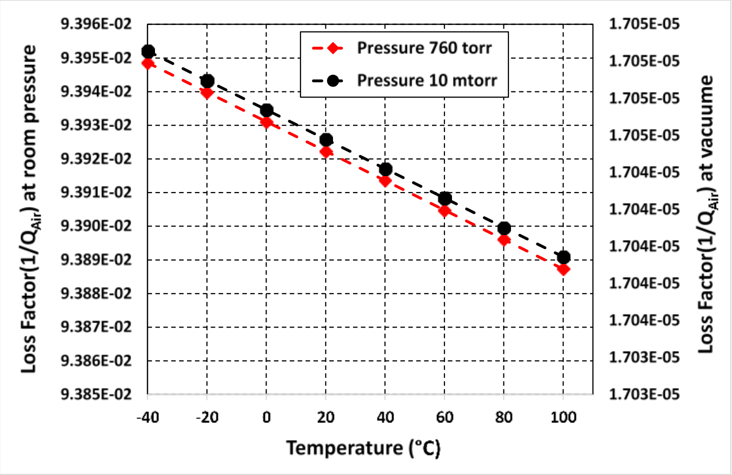

(a)

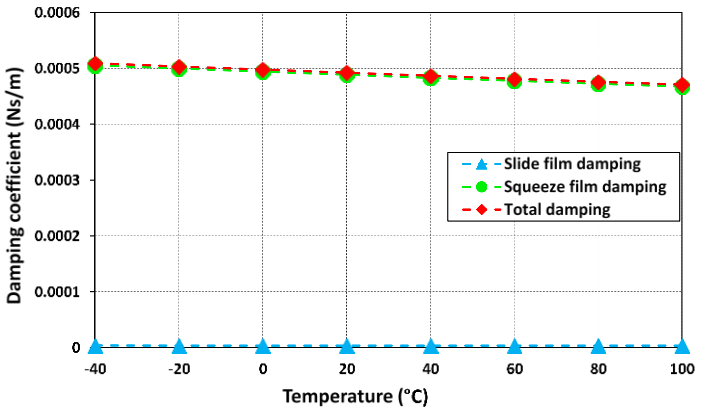

(b)

Figure 3.16: (a) Variation of Loss factor at resonance in temperature range of −40 ℃ to 100 ℃ for pressure value of 760 torr and 100 mtorr (b) Variation of squeeze and slide film damping in temperature range of -40 ℃ to 100 ℃

3.10 Accelerometer Response Characterization in the Presence of Shock

To analyze the response of proposed MEMS accelerometer to a shock load, different input shock pulses are applied. This input shock acceleration is applied in three different shape input pulses as shown in the Fig 3.17. To simplify the process we take the magnitude of input pulse as the shock amplitude. The profile of input shock pulse can be given as a half sine Eq. 12, a rectangular shape pulse Eq. 13 and a saw-tooth pulse Eq. 14. The mathematical expression for these input shock pulses [48] is given as,

$$a(t) = \sin\left(\frac{\pi t}{T}\right)u(t) + \sin\left(\frac{\pi(t-T)}{T}\right)u(t-T) \tag{12}$$

$$a(t) = \frac{2\left[r(t) - 2r\left(t-\frac{T}{2}\right) + r(t-T)\right]}{T} \tag{13}$$

$$a(t) = u(t) - u(t-T) \tag{14}$$

Where T is the duration of shock, $u(t)$ is the unit step function and $r(t)$ is the unit ramp function

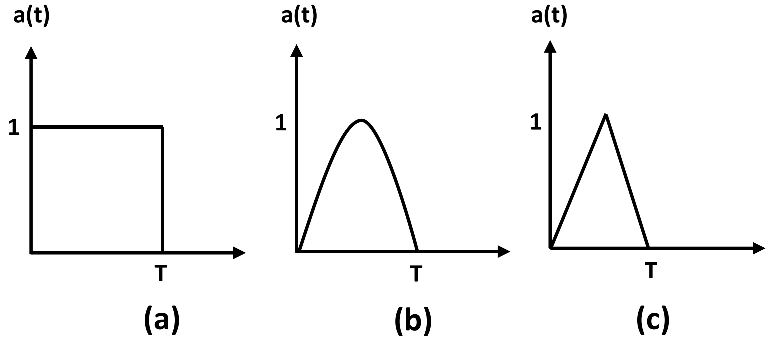

Figure 3.17: Input shock pulses to modal real shock loads (a) Rectangular input pulse, (b) Half sine input pulse, (c) Saw-tooth input pulse

The shock profile of half sine wave is assumed as input shock because it is very close to the shape of actual shock pulse [49,50]. Figure 3.18 (a) shows the profile of given input half sine shock pulse of 1000 *g* amplitude. To obtain the results of input shock pulses for proposed MEMS accelerometer, FE software ANSYS is used. The shock duration of rectangular and saw-tooth input shock pulses is varied from 1 *ms* to 10 *ms* to observe the time response of proposed MEMS accelerometer. Figure 3.18 (b) shows the time response for the input half sine shock pulse of duration 0.5 *ms* and response is observed for 15 *ms*. It is noted that the amplitude of response for 1000 *g* half sine shock input is 276 *µm* and settling time for the proof mass of proposed MEMS accelerometer is 8.3 *ms*.

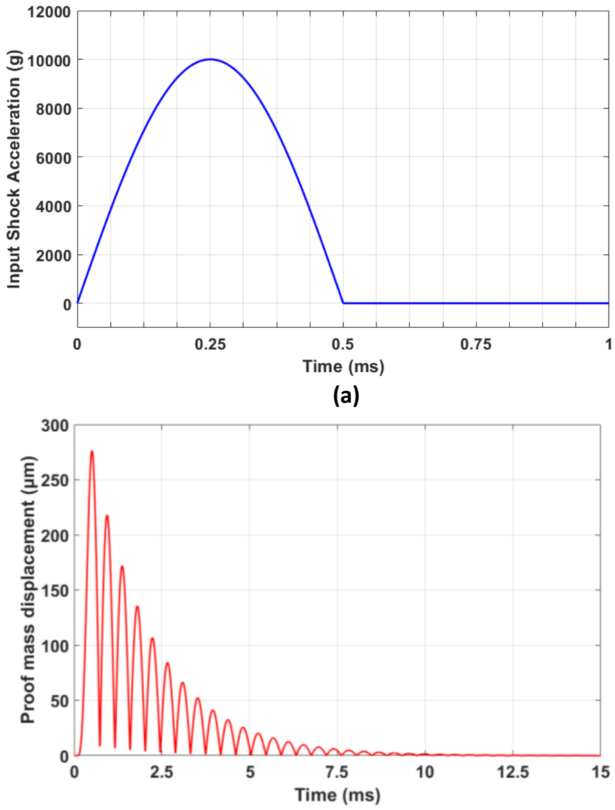

(a)

(b)

Figure 3.18: (a) 1000 *g* Shock input in the form of Half sine pulse (b) Shock response of proposed MEMS accelerometer for half sine input pulse of duration 0.5 *ms*

Figure 3.19 shows the time history response of the proposed MEMS accelerometer when rectangular and saw-tooth input shock pulses are applied. It can be observed that the time response of proposed MEMS accelerometer for an input shock duration of 10 *ms* is similar with the input shock pulse which is more prominent in case of saw-tooth pulse Fig. 3.19 (c) than restangular shock pulse Fig. 3.19 (a). It is observed in the Fig 3.19, that the proof mass displacement of proposed MEMS accelerometer for shock pulses of duration 1 *ms* of different shapes is greater than the same pulse shapes of duration 10 *ms*. Due to the sudden change in the bigining and end of rectangular shape input pulse, oscillating behavior of the proof mass is observed at that points as shown in Fig. 3.19 (a).

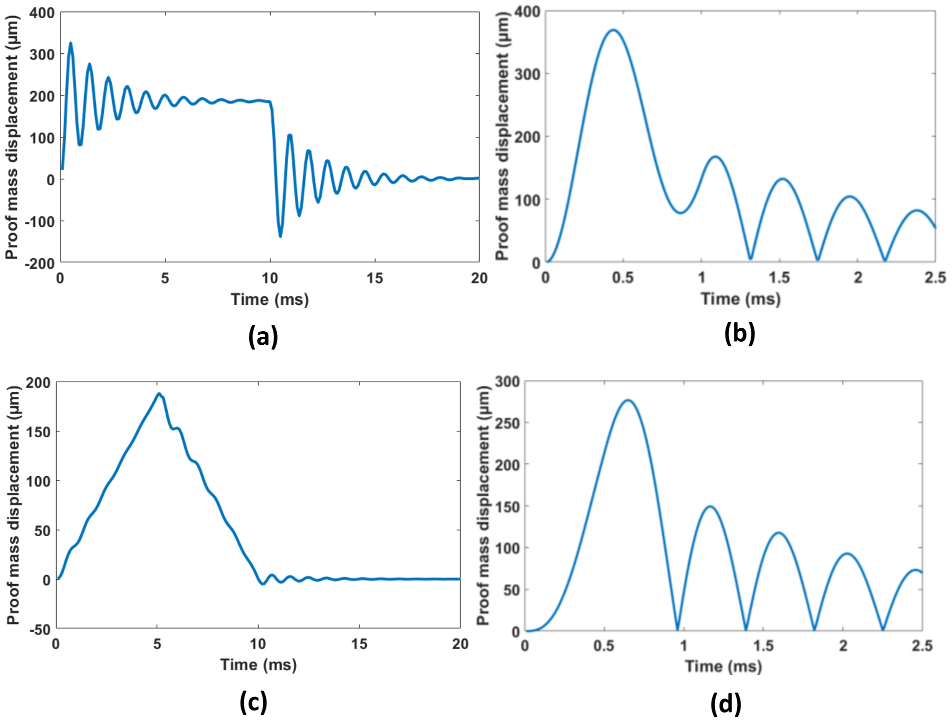

Figure 3.19: Shock response of proposed MEMS accelerometer for (a) rectangular pulse of duration 10 *ms* (b) rectangular pulse of duration 1 *ms* (c) saw-tooth pulse of duration 10 *ms* (d) saw-tooth pulse of duration 1 *ms*

3.11 Transient Analysis

Transient analysis is carried out using MATLAB integration with CoventorWare MEMS+ module. A step input acceleration of magnitude 15 *g* is applied to the accelerometer after an initial delay of 10 *ms*, the rise time of input signal is 1 *ms* and the pulse width is 3 *ms*. After the step input signal is removed the proof mass displacement stats to decrease due to the air damping between the fixed and moving combs. The oscillation reduces gradually and attain a stable value after ~ 45 *ms* which is the settling time of proposed MEMS accelerometer, the step input applied and the resulting response of the proof mass is shown in Fig. 3.20.

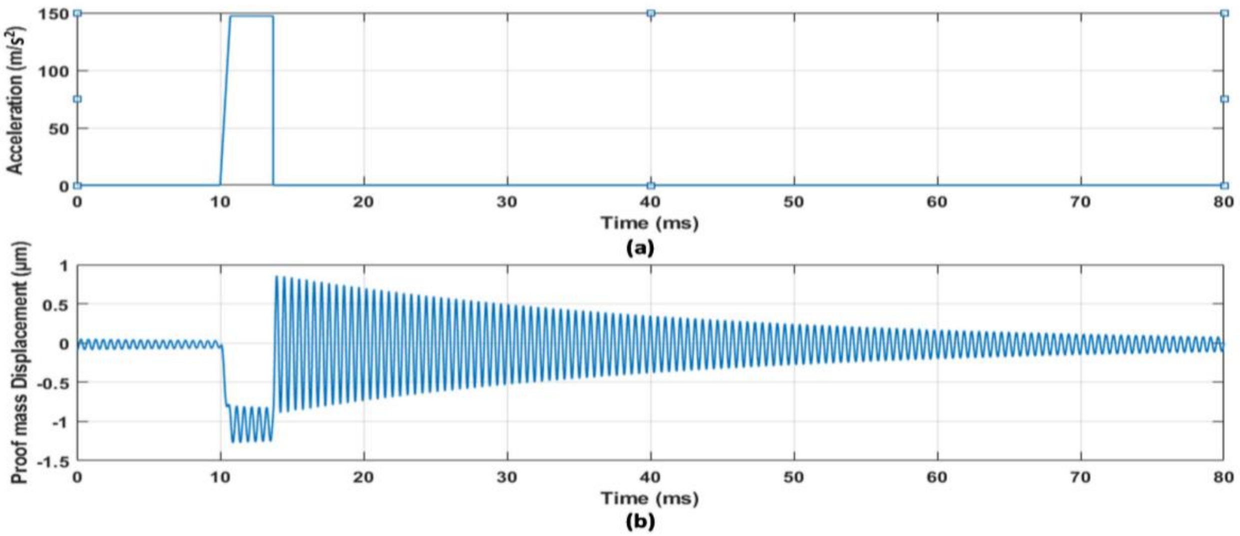

Fig. 3.20 (a) Input acceleration (b) Transient response of MEMS accelerometer.

Table 6: Specifications of Proposed MEMS Accelerometer

Parameter	**Value**
Structural Layer thickness (µm)	25
Size (μm^2)	3800×3800
Device sensitivity (*fF/g*)	31.5
Measurement range (±*g*)	34
Operating temperature (*℃*)	-40 to 100
Bandwidth (*Hz*)	400
Natural frequency (*KHz*)	1.866

Chapter 4: Dual Axis Capacitive MEMS Accelerometer Design using MIDIS Fabrication Process

4.1 Accelerometer Design

The proposed double axis MEMS accelerometer is configured by implementing the structural limitations of financially accessible microfabrication handle, MEMS Integrated Design for Inertial Sensors (MIDIS) displayed by Teledyne DALSA Semiconductor Inc. Figure 4.1 demonstrates the design of suggested MEMS accelerometer. Four groups of L shaped mechanical suspension bars was used to support the proof mass. The proof mass’ external edges are covered by the detecting combs which are organized by a maximum space of 10.5 µm and with a minimum space of 3.5 µm in a differential plot.

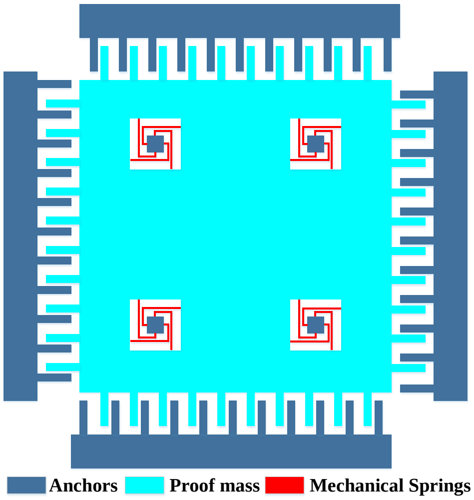

Figure 4.1: Diagram of dual axis capacitive accelerometer

4.2 Suspension Beams Stiffness Calculation

The stiffness of proposed mechanical suspension beams is given as,

$$k_b = \left(\frac{Ehw^3}{l^3}\right) \tag{15}$$

These four sets of beams are arranged around the proof mass to hold it in symmetric order as shown in figure 4.2. The equivalent mechanical stiffness of total springs is calculated as,

$$\mathrm{K} = \left(\frac{16Ehw^3}{(l_1^3+l_2^3+l_3^3)}\right) \tag{16}$$

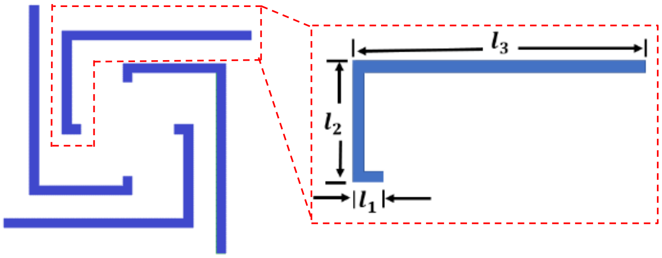

Fig. 4.2 Schematic of suspension spring

Table 7: Physical parameters

Physical Property	**Value**
parallel plates	145
Moving structure dimensions *mm2*	3.8 × 3.8
Thickness of structure $(\boldsymbol{t})$ μm	30
Parallel plate length (l_c) μm	300
Parallel plate width (w_c) μm	6
Common length (l_o) μm	290
Smaller gap (d_1) μm	3.5
Larger gap (d_2) μm	10.5
Equivalent spring constant (k) *N/m*	540
moving part mass (m) *N/m*	1.0998e-6

4.3 Analysis of Pull In

To observe the deflection of the moving part as a result of input acceleration, different sensing techniques are used. The most commonly used is capacitive technique because of its various advantages as compared to the other techniques. To observe the deflection of moving structure a gap and anti-gap scheme is used. A biasing voltage is applied between the rotor and stator parallel plates and the change in capacitance is observed. As an effect of applying this potential difference a electrostatic force is produces between the rotor and stator parallel sensing plates which attract the moving plates to stationary ones. The applied potential between the rotor and stator plates must be adjusted to avoid the pull in [41], whenever the applied potential rises to a specific predefined level, the rotor and stator parallel plates attract each other and stuck down. To avoid the parallel sensing plates from destruction the applied potential must be fixed under a certain limit. The applied potential difference where the pull in occurs can be calculated by;

$$V_{pull-in} = \sqrt{\frac{8kd_1^3}{27.l.t.N.\varepsilon}} \tag{17}$$

Where t shows the depth, d_1 represents the smaller gap, l denotes the common length of parallel sensing plates, k shows the mechanical suspension stiffness, free space permittivity is shown as ε number of rotor and stator pairs is given by N. A simulation performed in a simulation software shows that the pull in occurs at 11.1 volt however the analytical value calculated by Eq. 17 is 16.6 volt. Due the difference in the analytical and FEM stiffness values this difference in the potential difference for pull in occurs. The phenomenon of pull in is shown in the Fig. 4.3.

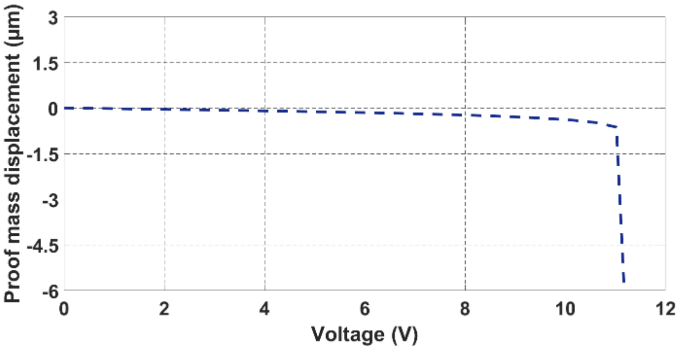

Fig. 4.3 Analysis of pull in

4.4 Noise Calculations

There are two types of noise accelerations, one is mechanical noise equivalent and other one is electrical noise equivalent which add up as total noise equivalent an given as [51]:

$$TNEA=\sqrt{MNEA^2+ENEA^2} \tag{18}$$

$$TNEA=\sqrt{(4\,k_B\,T\omega_0/Qm)+(c_{min}/s_c)} \tag{19}$$

Where Boltzmann constant is represented by k_B, temperature is represented as T, the scale factor is represented as s_c and the resolution is represented as c_{min}.

4.5 FEM simulations

4.5.1 Modal analysis

To observe the natural vibration shapes of the structure, a simulation is performed for modal analysis to observe the actual frequency of the device and the movements of the moving structure at these natural frequencies. The deflection of the moving structure at first two natural frequencies is shown in Fig. 4.4.

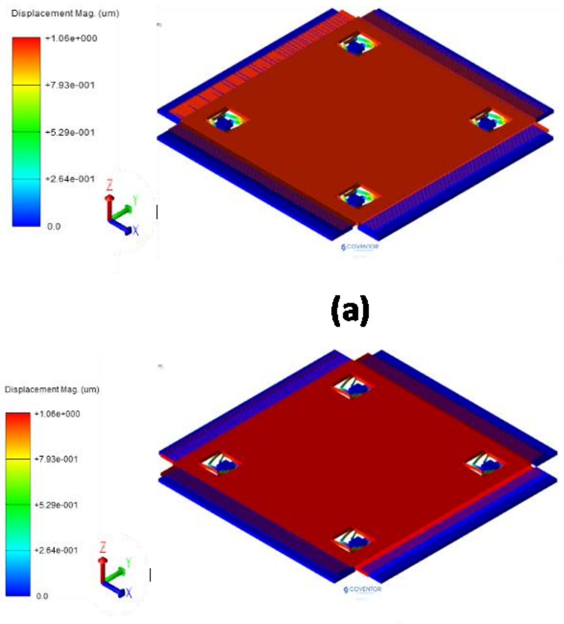

(a)

(b)

Fig. 4.4 Movements of moving part at (a) 1st natural frequency (b) 2^{nd} natural frequency

4.5.2 Frequency Response Analysis

Frequency response analysis is performed to estimate the movements of the moving mass under an input acceleration. To observe the behavior of the moving mass different input accelerations are applied and their corresponding deflection is observed. Fig. 4.5 demonstrate the movement of proof mass for a range of input frequencies for different range i.e. 10 to 50 *g* of input acceleration. Equations (8) and (9) from section 3.5 are utilized to calculate the damping value. The frequency response analysis shows that the maximum deposition of the proof mass occurs at the resonance frequency which is 23.1 µm and it is far beyond the initial gap of 3.5 µm between the parallel sensing plates so the operational range of the device is described from 0 to 400 Hz as in this region the movement of the proof mass is almost linear and its value is 1.01 µm for an input acceleration of 50 g.

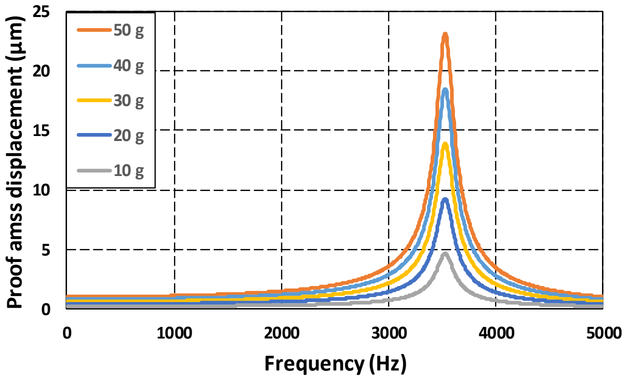

Fig. 4.5 Harmonic response analysis

4.5.3 Effect of Gravity

The effect of gravity on the device must be considered because these devices also experience a gravitational force. The deviation of the movable structure towards z-direction under the effect of gravity may modify the overlap region in the parallel sensing layers. The deflection caused by the gravity may change the value of spring constant of the device and its value should be estimated. Fig. 4.6 display the results of a simulation performed in a simulation software CoventorWare to characterize the effect of gravity. To observe the deflection of proof mass in the vertical direction an acceleration of value 1 g is directed towards z-direction. Under the effect of this applied input acceleration in z-direction the moving mass deflects a value of 17.6 nm which has minimal affect on the capacitance change of the device.

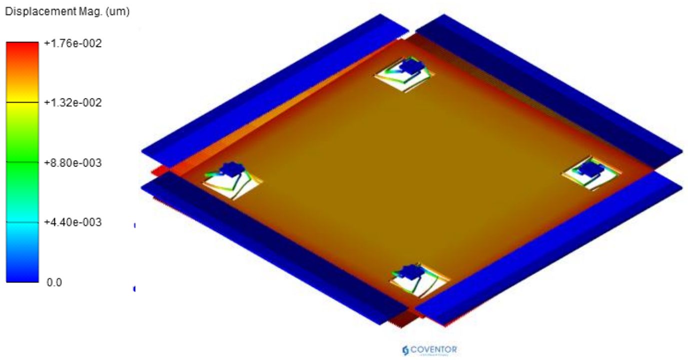

Fig. 4.6 Deflection due to gravitational force

4.5.4 Effects of temperature

To observe the effect of temperature on the device at different temperature values a simulation is performed in ANSYS. The results show the expansion and contraction of the moving structure for high and low values of temperature. This thermal expansion or contraction causes the initial gap between the parallel sensing plates to decrease as they are arranges in gap anti gap configuration which causes the decrease in the value of acceleration for pull in.

When the temperature increases or decreases the thermal expansion or contraction do not affect the change in capacitance because if the gap is decreasing on one side of the center, it is increasing simultaneously on the other side. In the range of -40 ℃ and 100 ℃ the thermal expansion and contraction of the device is shown in Fig. 4. The effect due to different values of temperature on the maximum acceleration as a result of change in the initial gap is shown Fig. 4.8.

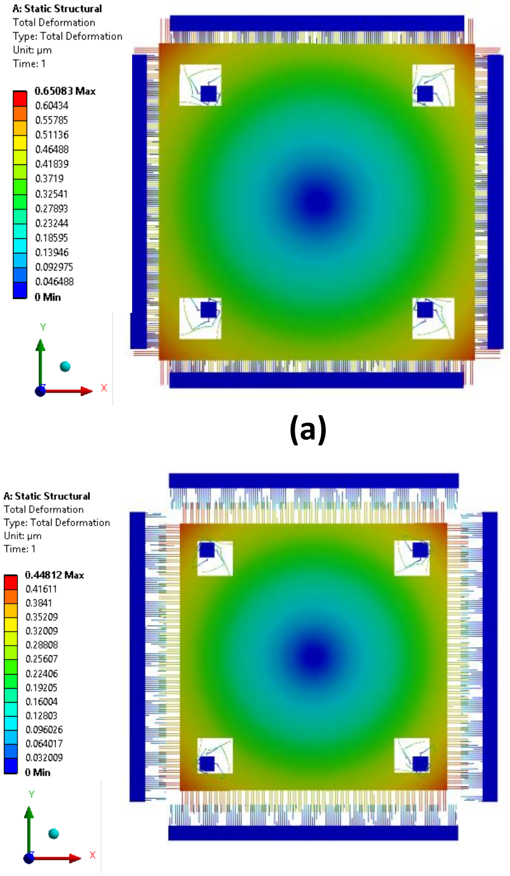

(a)

(b)

Fig. 4.7 Effect of temperature at (a) 100 °C (b) -40 °C

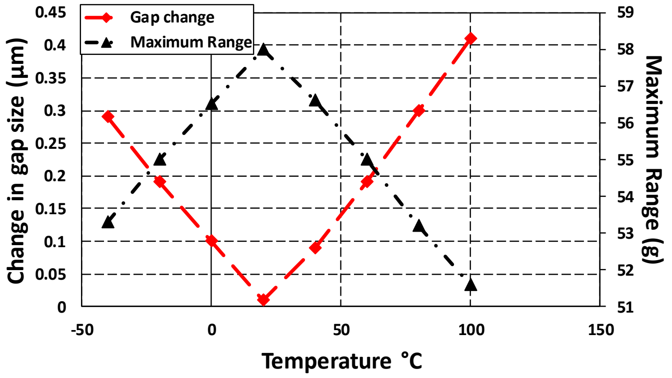

Fig. 4.8 Variation of input acceleration with temperature change

4.5.5 Analysis of Residual Stress

The residual stress in MEMS devices is generally developed either due to extrinsic factors like thermal property difference between different material layers and substrate and intrinsic factors including thin film grain size and growth rate variations during microfabrication. The residual stress in microbeams is superposition of a uniform in-plane stress and stress gradient that changes linearly along the beam thickness. The uniform in-plane stress results in an in-plane deformation and may eventually lead to buckling in microbeams with fixed boundary conditions. The stress gradient leads to the out-of-plane deformation in the microbeams. To study the effect of both in-plane residual stress and stress gradients on the final planarity of the MEMS accelerometer and on the resonant frequency, a complete FEM analysis was conducted in CovenetorWare. The effect of residual stress value on the resonance frequency in the range of -100 to 100 MPa is shown in Fig. 4.9. This result proves little influence on the resonant frequency of the device.

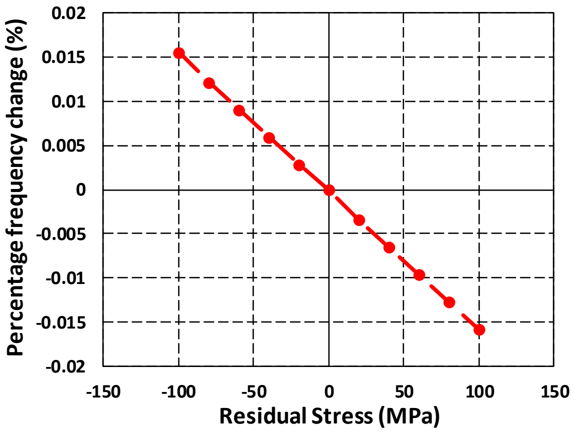

Fig. 4.9 Frequency variations with residual stress value

Table 8: Main Characteristics

Physical property	Value
Capacitive-Sensitivity (*fF/g*)	38
Operational-Range (±*g*)	50
Minimum-Resolution (*mg*)	2.5

Physical property	**Value**
Operating Temperature (℃)	-40 to 100
Operational Range (*Hz*)	400
Frequency at Resonance (*Hz*)	3528

4.5.6 Transient Response

To examine the result of the maximum input acceleration on the oscillations response and settling time of the MEMS accelerometer, a transient analysis in MEMS+ module of CoventorWare was performed. An input acceleration of 50 g magnitude with an initial delay of 5 ms is applied as shown in Fig. 10 (a). The analysis is carried out by considering the pressure conditions and total air dampening at room temperature, obtained through FEM analysis and discussed in Section 3.5. The results in Fig. 10 (b) shows that the oscillations in the proof mass of MEMS accelerometer decay   and displacement in the proof mass is 1.01 µm. The change in capacitance for this input acceleration is 2.9 *pF* and while using the resolution of the readout circuitry the capacitive sensitivity of the device is fF/g. The capacitance to voltage conversion is performed as;

$$V_o = 1.14 \times GAIN \times V2P25 \times \frac{S_c+(CS2-CS1)}{C_F} + V_{ref} \tag{20}$$

Where a constant value of *GAIN* is 2, capacitance for integration is represented as C_F , capacitive sensitivity as S_c and a constant value of 2.25 is assigned to *V2P25* and *Vref* .

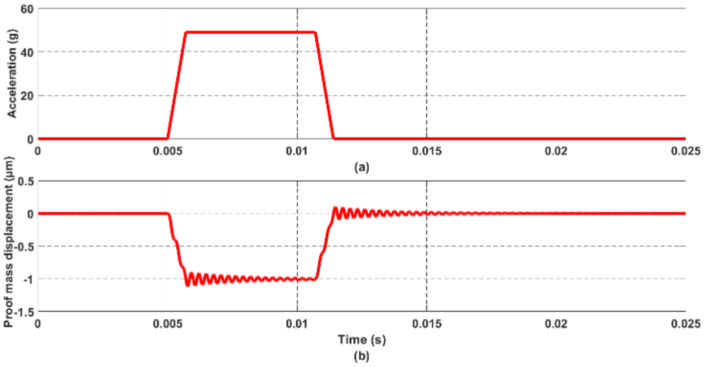

Fig. 4.10 Proof mass displacement for 50 g

4.5.7 Frequency Response Analysis for Temperature and Pressure

The proof mass transposition for various values of temperature and pressure is observed. The proof mass transposition for two distinct values of pressure is shown in the Fig. 4.11 which shows that the deflection of the proof mass decreases from 120 µm to 23.2 µm while changing the pressure value from 101 kPa to 20 kPa. There is negligible effect of temperature change on the proof mass displacement as shown in Fig. 4.12

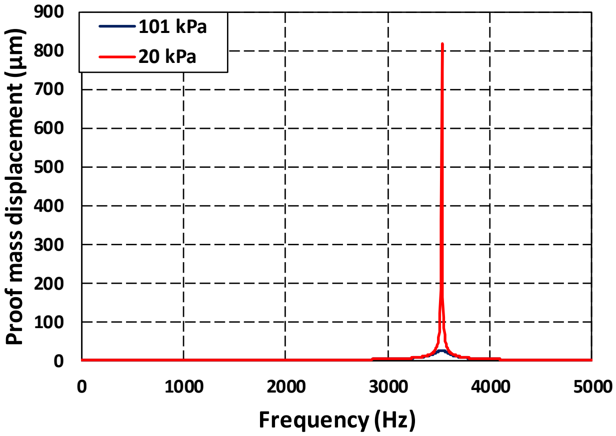

Figure. 4.11 Frequency response at different pressure values.

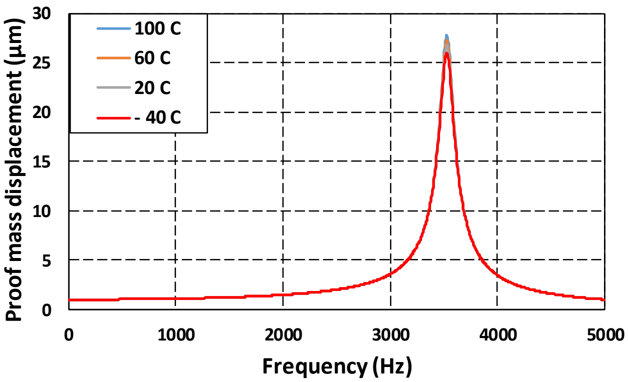

Fig. 4.12 Frequency curve at various values of temperature.

Chapter 5: Conclusion

In this research work a complete design for two different accelerometers is presented while considering two different fabrication processes. The first accelerometer is designed according to SOIMUMPS fabrication process while the second accelerometer follows design specifications of MIDIS fabrication process. The operating bandwidth of these designed devices is 0-400 *Hz* and capacitive sensitivities for design 1 and design 2 are 31.5 *fF/g* and 38 *fF/g*.

Parameter	**Design 1 (MIDIS Process)**	**Design 2 (SOIMUMPS Process)**
Structural Layer thickness (μm)	30	25
Size (μm^2)	3800×3800	3800×3800
Device sensitivity (*fF/g*)	38	31.5
Measurement range (±*g*)	50	34
Operating temperature (℃)	-40 to 100	-40 to 100
Bandwidth (*Hz*)	400	400
Natural frequency (*Hz*)	3528	1866

The operating temperature range of the accelerometers is -40 to 100 °*C*. The effect of input acceleration frequency, temperature variations and air compulsion changes on the air dampening and hence the quality factor of MEMS accelerometer is presented. The results showed that for the proposed MEMS accelerometer, the viscous air damper force is the prime power diffusion mechanism and the quality factor increases sequentially with the increase in both operating temperature and air pressure. In addition to air dampening, the impact of thermoelastic damping (TED) on the quality factor of MEMS accelerometer is analyzed which showed that TED damping depends significantly on the thermal stability of the structural matter in addition to mechanical design of MEMS accelerometer. The results show that by considering constant material properties, the TED based quality factor decreases with an increasing temperature while for temperature dependent properties, the effect of increase in the operating temperature on the quality factor is opposite i.e. quality factor increases nonlinearly with an increasing temperature.

The pull-in analysis is performed to observe the maximum biased voltage that might be applicable before the parallel sensing plates stuck to each other due to the strong electrostatic force. The end stops are designed at the all four edges of the proof mass corners to avoid the destruction of the sensing combs in presence of shock. The temperature effects on different performance parameters of the device are observed. The consequences of -40 to 100 *°C* temperature range is noticed on the deformation of the sensing parallel moving plates and resulting change in the capacitance of the device.

The input acceleration range of the accelerometer in -40 to 100 *°C* range of temperature is observed i.e. ±34 *g* for accelerometer designed using SOIMUMPs fabrication process. The impact of pressure along with temperature onto the frequency response of the device is observed for different values of temperature and pressure. The voltage sensitivity of the device is observed by integrating the readout circuitry in MATLAB Simulink environment and behavior of the accelerometer is observed under various shock conditions by applying different shaped input pulses. The responsivenes of the proof mass for various temperature and pressure values is observed which shows that there is a minimal effect of temperature, however the pressure values of 10 *mTorr* and 760 *Torr* have affected the output response as changing pressure strongly changes the damping conditions.

The difference in the sensitivities of these two designed accelerometers is because of the difference in the compactness of the layers of two different fabrication processes, the stiffness of the mechanical suspension beams holding the proof mass, number of parallel sensing plates their dimensions and the initial gaps between them.

Completion Certificate

It is certified that the contents of thesis document titled "***Design of Capacitive Micro-Electro-Mechanical-Systems (MEMS) Accelerometer, Considering Residual Stress, Temperature Variations and Thermoelastic Damping***" submitted by NS Muhammad Ahmad Raza Tahir, Registration No. 0000278052 have been found satisfactory in all respects as per the requirements of Main Office, NUST (Exam branch).

Supervisor: ___________________
Dr. Muhammad Mubasher Saleem
Date: ____ April, 2020

References

[1] Feynman, R. P. (1992). There's plenty of room at the bottom [data storage]. *Journal of microelectromechanical systems*, 1(1), 60-66.

[2] Mohammed, Z., Gill, W. A., Rasras, M.: 'Double-comb-finger design to eliminate cross-axis sensitivity in a dual-axis accelerometer', *IEEE Sensors* Letters, 2017, 1 (5), 1-4

[3] Colinjivadi, K. S., Lee, J. B. and Draper, R. (2008). Viable cell handling with high aspect ratio polymer chopstick gripper mounted on a nano precision manipulator. *Microsystem Technologies*, 14(9-11), 1627-1633.

[4] Khazaai, J. J., Qu, H., Shillor, M. and Smith, L. (2011, October). Design and fabrication of electro-thermally activated micro gripper with large tip opening and holding force. In *SENSORS, 2011 IEEE* (pp. 1445-1448). IEEE.

[5] Chen, D. S., Yin, C. Y., Lai, R. J. and Tsai, J. C. (2009, January). A multiple degrees of freedom electrothermal actuator for a versatile MEMS gripper. In 2009 IEEE 22nd International Conference on Micro Electro Mechanical Systems (pp. 1035-1038). IEEE.

[6] Cowen, A., Hames, G., Monk, D., Wilcenski, S. and Hardy, B. (2011). SOIMUMPs design handbook. *MEMSCAP Inc*, 2002-2011.

[7] Zhang, R., Chu, J., Wang, H. and Chen, Z. (2013). A multipurpose electrothermal microgripper for biological micro-manipulation. Microsystem technologies, 19(1), 89-97.

[8] Kim, K., Liu, X., Zhang, Y. and Sun, Y. (2008). Nanonewton force-controlled manipulation of biological cells using a monolithic MEMS microgripper with two-axis force feedback. *Journal of micromechanics and microengineering,* 18(5), 055013.

[9] Beyeler, F., Neild, A., Oberti, S., Bell, D. J., Sun, Y., Dual, J. and Nelson, B. J. (2007). Monolithically fabricated microgripper with integrated force sensor for manipulating microobjects and biological cells aligned in an ultrasonic field. *Journal of microelectromechanical systems,* 16(1), 7-15.

[10] Volland, B. E., Heerlein, H. and Rangelow, I. W. (2002). Electrostatically driven microgripper. *Microelectronic engineering,* 61, 1015-1023.

[11] Roch, I., Bidaud, P., Collard, D. and Buchaillot, L. (2003). Fabrication and characterization of an SU-8 gripper actuated by a shape memory alloy thin film. *Journal of Micromechanics and Microengineering,* 13(2), 330.

[12] Yang, S. and Xu, Q. (2017). A review on actuation and sensing techniques for MEMS-based microgrippers. *Journal of Micro-Bio Robotics*, 13(1-4), 1-14.

[13] Solano, B. and Wood, D. (2007). Design and testing of a polymeric microgripper for cell manipulation. *Microelectronic Engineering,* 84(5-8), 1219-1222.

[14] Khazaai, J. J., Qu, H., Shillor, M. Smith, L. (2011, October). Design and fabrication of electro-thermally activated micro gripper with large tip opening and holding force. In *SENSORS, 2011 IEEE* (pp. 1445-1448). IEEE.

[15] Chang, H., Zhao, H., Ye, F., Yuan, G., Xie, J., Kraft, M. and Yuan, W. (2014). A rotary comb-actuated microgripper with a large displacement range. *Microsystem technologies,* 20(1), 119-126.

[16] Boudaoud, M., Haddab, Y. and Le Gorrec, Y. (2010, October). Modelling of a MEMS-based microgripper: application to dexterous micromanipulation. In 2010 IEEE/RSJ International Conference on Intelligent Robots and Systems (pp. 5634-5639). *IEEE.*

[17] Munasinghe, K. C., Bowatta, B. G. C. T., Abayarathne, H. Y. R., Kumararathna, N., Maduwantha, L. K. A. H., Arachchige, N. M. P. and Amarasinghe, Y. W. R. (2016, April). New MEMS based micro gripper using SMA for micro level object manipulation and assembling. In *2016 Moratuwa Engineering Research Conference* (MERCon) (pp. 36-41). IEEE.

[18] AbuZaiter, A., Nafea, M.and Ali, M. S. M. (2016). Development of a shape-memory-alloy micromanipulator based on integrated bimorph microactuators. *Mechatronics,* 38, 16-28.

[19] Park, J. and Moon, W. (2003). A hybrid-type micro-gripper with an integrated force sensor. *Microsystem technologies*, 9(8), 511-519.

[20] Jeon, C. S., Park, J. S., Lee, S. Y. and Moon, C. W. (2007). Fabrication and characteristics of out-of-plane piezoelectric micro grippers using MEMS processes. Thin Solid Films, 515(12), 4901-4904.

[21] Kim, W. H., Park, J. S., Shin, K. S., Park, K. B., Seong, W. K. and Moon, C. W. (2005). Simulation and fabrication of silicon micro-grippers actuated by piezoelectric actuator. In Materials Science Forum (Vol. 475, pp. 1885-1888). Trans Tech Publications Ltd.

[22] Kim, D. H., Lee, M. G., Kim, B. and Sun, Y. (2005). A superelastic alloy microgripper with embedded electromagnetic actuators and piezoelectric force sensors: a numerical and experimental study. Smart materials and structures, 14(6), 1265.

[23] Chen, D. S., Yeh, P. F., Chen, Y. F., Tsai, C. W., Yin, C. Y., Lai, R. J. and Tsai, J. C. (2013). An electrothermal actuator with two degrees of freedom serving as the arm of a MEMS gripper. *IEEE Transactions on Industrial Electronics*, 61(10), 5465-5471.

[24] Sergio, M., Manaresi, N., Tartagni, M., Guerrieri, R. and Canegallo, R. (2002, June). A textile based capacitive pressure sensor. In SENSORS, 2002 IEEE (Vol. 2, pp. 1625-1630). IEEE.

[25] Ko, C. T., Tseng, S. H. and Lu, M. S. C. (2006). A CMOS micromachined capacitive tactile sensor with high-frequency output. *Journal of Microelectromechanical Systems,* 15(6), 1708-1714.

[26] Dürig, U. (2005). Fundamentals of micromechanical thermoelectric sensors. Journal of Applied Physics, 98(4), 044906.

[27] Zhu, Y., Bazaei, A., Moheimani, S. O. R. and Yuce, M. R. (2010). A micromachined nanopositioner with on-chip electrothermal actuation and sensing. *IEEE Electron device letters,* 31(10), 1161-1163.

[28] Piriyanont, B., Fowler, A. G. and Moheimani, S. R. (2015). Force-controlled MEMS rotary microgripper. *Journal of Microelectromechanical Systems*, 24(4), 1164-1172.

[29] Mei, T., Ge, Y., Chen, Y., Ni, L., Liao, W. H., Xu, Y. and Li, W. J. (1999, January). Design and fabrication of an integrated three-dimensional tactile sensor for space robotic applications. In Technical Digest. IEEE International MEMS 99 Conference. Twelfth IEEE International *Conference on Micro Electro Mechanical System*s (Cat. No. 99CH36291) (pp. 112-117). IEEE.

[30] Hasegawa, Y., Shikida, M., Shimizu, T., Miyaji, T., Sasaki, H., Sato, K. and Itoigawa, K. (2004). Amicromachined active tactile sensor for hardness detection. *Sensors and Actuators A: physical*, 114(2-3), 141-146.

[31] Xu, Q. (2015). Design, fabrication, and testing of an MEMS microgripper with dual-axis force sensor. IEEE Sensors Journal, 15(10), 6017-6026.

[32] Han, K., Lee, S. H., Moon, W. and Park, J. S. (2006, October). Fabrication of the micro-gripper with a force sensor for manipulating a cell. In 2006 SICE-ICASE International Joint Conference (pp. 5833-5836). IEEE.

[33] Yazdi, Navid, Farrokh Ayazi, and Khalil Najafi. "Micromachined inertial sensors." Proceedings of the IEEE 86.8 (1998): 1640-1659.

[34] Chattaraj, D., Swamy, K. B. M., Sen, S.: ‘Design and analysis of dual axis MEMS accelerometer’, In 2007 International Workshop on Physics of Semiconductor Devices, IEEE., 2007, pp. 718-720

[35] Tsai, M. H., Liu, Y. C., Fang, W.: ‘A three-axis CMOS-MEMS accelerometer structure with vertically integrated fully differential sensing electrodes’, *Journal of Microelectromechanical Systems*, 2012, 21, (6), pp. 1329-1337

[36] Lo, S. C., Chan, C. K., Lai, W. C., Wu, M., Lin, Y. C., Fang, W.: ‘Design and implementation of a novel poly-Si single proof-mass differential capacitive-sensing 3-axis accelerometer’, In 2013 Transducers Eurosensors XXVII: The 17th International Conference on Solid-State Sensors, Actuators and Microsystems. IEEE. pp. 1819-1822

[37] Serrano, D. E., Jeong, Y., Keesara, V., K. Sung, W., Ayazi, F.: ‘Single proof-mass tri-axial pendulum accelerometers operating in vacuum’, In 2014 IEEE 27th International Conference on Micro Electro Mechanical Systems (MEMS). IEEE. pp. 28-31

[38] Khan, S., Ananthasuresh, G. K.: ‘Improving the sensitivity and bandwidth of in-plane capacitive microaccelerometers using compliant mechanical amplifiers’, *Journal of Microelectromechanical Systems,* 2014, 23, (4), pp. 871-887

[39] Shan, X., Angeles, J., Forbes, J. R.: ‘Design of a biaxial high frequency-ratio low-g MEMS accelerometer’, *Microsystem Technologies*, 2018, 24, (9), pp. 3851-3861

[40] Vemuri, S. (2000). Behavioral Modeling in Viscous Damping in MEMS. CARNEGIE-MELLON UNIV PITTSBURGH PA DEPT OF ELECTRICAL AND COMPUTER ENGINEERING.

[41] Somà, A., Saleem, M. M., & De Pasquale, G. (2016). Effect of creep in RF MEMS static and dynamic behavior. Microsystem Technologies, 22(5), 1067-1078. Zener, C. (1937). Internal friction in solids. I. Theory of internal friction in reeds. Physical review, 52(3), 230.

[42] Hossain, Syed T., Stewart McWilliam, and Atanas A. Popov. "An investigation on thermoelastic damping of high-Q ring resonators." International Journal of Mechanical Sciences 106 (2016): 209-219.

[43] Kim, B., Hopcroft, M. A., Candler, R. N., Jha, C. M., Agarwal, M., Melamud, R., ... & Kenny, T. W. (2008). Temperature dependence of quality factor in MEMS resonators. Journal of Microelectromechanical systems, 17(3), 755-766.

[44] Miller, D. C., Boyce, B. L., Dugger, M. T., Buchheit, T. E., & Gall, K. (2007). Characteristics of a commercially available silicon-on-insulator MEMS material. Sensors and Actuators A: Physical, 138(1), 130-144.

[45] Wachtman Jr, J. B., Tefft, W. E., Lam Jr, D. G., & Apstein, C. S. (1961). Exponential temperature dependence of Young's modulus for several oxides. Physical review, 122(6), 1754.

[46] Gysin, U., Rast, S., Ruff, P., Meyer, E., Lee, D. W., Vettiger, P., & Gerber, C. (2004). Temperature dependence of the force sensitivity of silicon cantilevers. Physical review B, 69(4), 045403.

[47] Veijola, T., & Raback, P. (2007). Methods for solving gas damping problems in perforated microstructures using a 2D finite-element solver. Sensors, 7(7), 1069-1090.

[48] Younis, Mohammad I., Fadi Alsaleem, and Daniel Jordy. "The response of clamped–clamped microbeams under mechanical shock." International Journal of Non-Linear Mechanics 42.4 (2007): 643-657.

[49] Béliveau, A., Spencer, G. T., Thomas, K. A., & Roberson, S. L. (1999). Evaluation of MEMS capacitive accelerometers. IEEE Design & Test of Computers, 16(4), 48-56.

[50] Srikar, V. T., & Senturia, S. D. (2002). The reliability of microelectromechanical systems (MEMS) in shock environments. Journal of Microelectromechanical Systems, 11(3), 206-214.

[51] P. Monajemi, F. Ayazi, “Design optimization and implementation of a microgravity capacitive HARPSS accelerometer,” IEEE Sensors Journal, vol. 6, no. 1, pp. 39-46, 2006.

[52]